Revision 2

U-Pb LA-ICP-MS dating of apatite in mafic rocks: evidence for a major magmatic event at the Devonian-Carboniferous boundary in the Armorican Massif (France)

Anthony Pochon[1], Marc Poujol[1], Eric Gloaguen[2, 3], Yannick Branquet[1, 2], Florence Cagnard[2,3], Charles Gumiaux[2], Denis Gapais[1]

[1] Géosciences Rennes, UMR CNRS 6118, Université de Rennes 1, OSUR, Campus de Beaulieu, 35042 Rennes Cedex, France

[2] Institut des Sciences de la Terre d'Orléans, UMR 7327, Université d'Orléans, Campus Géosciences, 1A rue de la Férollerie, 45071 Orléans Cedex 2, France

[3] Bureau de Recherche Géologique et Minière (BRGM), UMR 7327, 3 avenue Claude-Guillemin, BP 36009, 45060 Orléans Cedex 02, France

Words count
Abstract = 286
Main text = 6183 (without title, abstract and keywords)
Tables = 4
Figures = 9
Supplementary data = 1
References = 81

This is a preprint, the final version is subject to change, of the American Mineralogist (MSA)
Cite as Authors (Year) Title. American Mineralogist, in press.
(DOI will not work until issue is live.) DOI: http://dx.doi.org/10.2138/am-2016-5736

Abstract

Apatite is a ubiquitous accessory mineral found in most magmatic rocks and is often the only U-bearing mineral available to date mafic rocks because primary zircon and/or baddeleyite are not present. In this paper, U-Pb LA-ICP-MS dating of apatite was applied to 7 different dike and sill samples of dolerite from the Variscan belt of Brittany (Armorican Massif, western France). These dolerites, which are characterized by a within-plate tholeiite geochemical signature, are organized in several dense swarms across the belt. Their geochemical compositions are rather homogeneous although they intrude a large geographical area subdivided into several domains each characterized by different tectono-metamorphic settings. Their emplacement ages were so far poorly constrained due to the difficulty to date these mafic rocks using either the $^{40}Ar/^{39}Ar$ or the U-Pb methods on classical minerals like mica, plagioclase or zircon. Although the closure temperature of apatite is lower than the emplacement temperature of the magma, physical models show that the time needed to solidify and cool these mafic dikes and sills below the apatite closure temperature is basically of the order of 100 years or less. Consequently, the U-Pb dates obtained on apatite can be interpreted as the emplacement ages for these mafic intrusions. Our results demonstrate that, in all cases, the apatite grains do carry enough radiogenic Pb to be dated by in-situ U-Pb analyses and yield a ^{207}Pb-corrected mean age of 363.4 ± 5.8 Ma. These results reveal the existence of a major and short-lived magmatic event in the Variscan belt of Brittany during the Devonian-Carboniferous transition, a feature further highlighted by field evidence. Beyond the geological implications of these results, U-Pb LA-ICP-MS dating of apatite appears to represent an ideal tool to date small size mafic intrusions.

Keywords: Apatite, LA-ICP-MS, U-Pb dating, mafic rocks, French Variscan belt.

Introduction

Apatite is a common accessory mineral in metamorphic, sedimentary, mafic and felsic igneous rocks (Watson 1979, 1980; Green and Watson 1982; Harrison and Watson 1984; Piccoli and Candela 2002; Spear and Pyle 2002; Webster and Piccoli 2015). The structure of apatite is very stable and can accommodate a number of substitutions including Pb (McConnell 1938) and U which may substitute for Ca via a charge coupled substitution involving a Ca-deficiency (Oosthuyzen and Burger 1973; Baumer et al. 1983; Hugues and Rakovan 2002). Furthermore, it is the most ubiquitous U-bearing mineral in mafic rocks, unlike zircon or baddeleyite, and can consequently represent a powerful tool for U-Pb geochronology. Empirical and experimental closure temperatures for Pb diffusion in apatite are between ca. 375°C and 550°C (Cherniak et al. 1991; Chamberlain and Bowring 2000; Harrison et al. 2002; Schoene and Bowring 2007; Cochrane et al. 2014), which is a range of temperatures that is lower than the U-Pb closure temperatures for zircon, baddeleyite, and titanite but higher than the one for Ar-Ar in biotite (Reiners et al. 2005 and references therein). Furthermore, in small-size mafic bodies (dikes, sills and plugs), the K-Ar whole rock and $^{40}Ar/^{39}Ar$ on plagioclase methods are often hard to apply either because of the excess Ar acquired from the host-rock or because of the loss or excess of K resulting from chemical weathering and/or alteration (Ruffet et al. 1992, Kelley 2002, Faure and Mensing 2005). The $^{40}Ar/^{39}Ar$ dating of biotite and amphibole can be used but these minerals are rarely present in mafic dikes and sills. Because of its medium-range closure temperature, U-Pb dating of apatite may not appear to be the best choice to date the emplacement of hot and large, slowly cooling, mafic bodies. However, for mafic dikes or sills, objects that are limited in size with a fast cooling rate, it may represent a very pertinent mineral to use provided these rocks have not experienced a reheating event above the closure temperature of apatite.

Apatite was first dated with the U-Pb method by Aldrich et al. (1955) and Tilton et al. (1955). However apatite accommodates significant amounts of common Pb in its crystal lattice (Chamberlain and Bowring 2000; Hugues and Rakovan 2002; Cochrane et al. 2014) and has typically low U and radiogenic Pb concentrations and, consequently, rather low radiogenic Pb/common Pb ratios. It is therefore necessary to perform a so-called common Pb correction in order to distinguish the radiogenic Pb from the common Pb. Although this problem can be easily resolved using the isotope dilution thermal ionization mass spectrometry (ID-TIMS) technique, it becomes more problematic for in-situ analyses (secondary ion mass spectrometry (SIMS) or laser ablation inductively coupled plasma mass spectrometry (LA-ICP-MS)). Indeed, in-situ analysis requires the use of a standard (most often an external standard, i.e. a matrix-matching mineral with a known age) in order to correct the raw data for the analytical biases inherent to this technique, namely the downhole fractionation and the instrumental drift. Although it is easy to find high quality natural and concordant standards for minerals that carry no common Pb (such as zircon, monazite, or baddeleyite), it is very difficult for common Pb bearing minerals such as apatite. Therefore, these standards, while potentially usable to correct the analyses for the instrumental biases, do often carry common Pb, which in turns means that they are not concordant. Thus, a common Pb correction also needs to be applied to the standards themselves. Recent developments using either MC-ICP-MS and/or new data treatment, as well as the discovery of age homogeneous apatite standards (Storey et al. 2007; Carrapa et al. 2009; Thomson et al. 2012; Chew et al. 2011, 2014) have considerably improved the applicability of U-Pb dating of apatite by in-situ LA-ICP-MS analysis. In this study, we implemented a new approach developed by Chew et al. (2014) using apatite standards carrying variable common Pb.

This paper focuses on the application of U-Pb dating of apatite by in-situ LA-ICP-MS in order to obtain the emplacement ages of various dikes and sills of dolerite from the Armorican

Massif, which is located in the western part of French Variscan belt. These mafic rocks are widespread in the region and form several swarms of dikes crosscutting a Neoproterozoic to Paleozoic sedimentary series. Some dikes are spatially associated with Sb and Au mineralization, especially in the central part of the Armorican Massif (Chauris et al. 1985; Pochon et al. 2016). This magmatism, described as characteristic of within-plate tholéiite, is constrained by some previous studies (Le Gall and Mary 1983; Mary and Le Gall 1985; Houlgatte et al. 1988; Lahaye et al. 1995; Le Gall 1999; Aïfa et al. 1999) but the precise timing of the emplacement of these mafic rocks remains poorly constrained, in particular because of the scarcity of minerals suitable for dating. Apatite is present as an accessory mineral in all of these rocks and appears to represent the best candidate to date them. Petrography, whole rock analyses, and apatite geochemical analyses have been performed on samples from these rocks in order to check for their degrees of alteration/weathering and to confirm a magmatic origin for the apatite grains before performing the LA-ICP-MS analyses.

Geological background

Main structural features

The Armorican Massif is located in western France and is part of the West European Variscan belt which resulted from the continental collision between the Gondwana and Laurussia plates and the Armorica microplate (Ballèvre et al. 2009, 2014). This collision began during the late Devonian and continued until the early Carboniferous (Matte 1986, Ballèvre et al. 2014). The Armorican Massif comprises three main domains with contrasted structural styles and deformation histories: the North Armorican, Central Armorican, and South Armorican domains. These domains are bounded by two dextral crustal-scale shear zones, the North Armorican Shear

Zone and the South Armorican Shear Zone (NASZ and SASZ respectively, Fig. 1). The North Armorican domain was essentially affected by Neoproterozoic deformations and constituted a part of the upper brittle crust un-metamorphosed during the Variscan orogeny (Brun et al. 2001). The Central Armorican domain is made of Late Neoproterozoic to upper Paleozoic sediments affected by moderate deformations (Gumiaux et al. 2004a, 2004b) and a low-grade regional metamorphism during the Variscan orogeny. The maximum temperature reached is estimated to be close to 250-300°C, based on vitrinite reflectance (Donnot et al. 1973), chloritoid-bearing slate occurrences (Le Corre 1969), the illite crystallinity (Le Corre 1975), and the chlorite geothermometer (Gloaguen et al. 2007). The South Armorican domain belongs to the internal metamorphic zones of the Variscan belt. It was affected by crustal thickening during late-Devonian to Carboniferous times, with a high pressure-low temperature event at ca. 360 Ma (Bosse et al. 2000; 2005), followed by late-Carboniferous extension (Gapais et al. 1993, 2015).

Magmatism in the Armorican Massif

Several magmatic events occurred during the Paleozoic in the Armorican Massif. These are first represented by bimodal magmatism and volcanism during the late Cambrian-early Ordovician, featuring calc-alkaline and rare peraluminous series (Ballèvre et al. 2014 and references therein). The late Cambrian event is best developed in the North Armorican domain, whereas the early Ordovician event is best developed in the Central and South Armorican domains.

Numerous Variscan granitoids have been emplaced in the Armorican Massif and are characterized by different geochemical associations (Capdevila 2010; Tartèse and Boulvais 2010; Tartèse et al. 2011a, 2011b; Ballouard et al. 2015). According to Capdevila (2010), 5 main

146 associations are currently recognized: i) a ca. 370 Ma (U-Pb method on zircon; Cuney et al.
147 1993) calc-alkaline association containing orogenic biotite-hornblende granites resulting from the
148 partial melting of an enriched mantle; ii) a ca. 330 Ma Mg-potassic metaluminous association that
149 includes mafic to intermediate rocks and porphyroid biotite-hornblende monzogranites (e.g.
150 Plouaret granite, 329 ± 5 Ma - whole-rock Rb-Sr, Peucat et al. 1984); iii) a Mg-potassic
151 peraluminous association made up of monzodiorite with a mantle origin, monzogranite and
152 cordierite granite from partial melting of metasediments; and iv) a ca. 316-310 Ma two mica
153 peraluminous leucogranites formed by the partial melting of a similar metasedimentary sources
154 (Tartèse and Boulvais 2010), e.g. the Guérande leucogranite (309.7 ± 1.3 Ma by U-Pb method on
155 zircon and monazite; Ballouard et al. 2015) and the Lizio granite (316 ± 1.3 Ma by U-Pb on
156 zircons, Tartèse et al. 2011b); and v) ca. 300 Ma red monzogranites and porphyroid syenogranites
157 (e.g. the Ploumanac'h granite, 303 ± 15 Ma - whole-rock Rb-Sr, Vidal 1980).

158 The North and Central Armorican domains are also marked by a dense swarm of dikes
159 and sills of dolerite that intrude the Late Proterozoic to Devonian sediments (Velde 1970; Ruffet
160 et al. 1992; Lahaye et al. 1995; Aïfa et al. 1999; Le Gall 1999). They are spatially distributed in
161 several groups (Fig. 1) defined by Le Gall (1999). The Mancellia and Saint-Malo group consists
162 of wide and dense swarms of dolerite dikes oriented N-S. The Laval Basin group comprises dikes
163 and sills of dolerite crosscutting Silurian and Devonian sediments and basaltic flows emplaced
164 within early Carboniferous series (Plaine 1976; Houlgatte et al. 1988; Pelhate 1994). The
165 Martigné-Ferchaud group consists of dike swarms striking N140° and spatially associated with
166 Sb mineralization (Chauris et al. 1985; Pochon et al. 2016). According to Le Gall (1999), the
167 dolerites of these groups present homogeneous geochemical compositions and appear to be
168 similar in composition to the thick mafic and felsic volcanosedimentary sequences of the
169 Châteaulin Basin in the western part of the Armorican Massif (Pelhate 1994; Caroff et al. 1996).

They are interpreted as within-plate tholeiites emplaced during a distensive/transtensive event or during a transpressive phase prior to the late Carboniferous (Le Gall and Mary 1983; Mary and Le Gall 1985; Houlgatte et al. 1988; Lahaye et al. 1995; Le Gall 1999; Rolet et al. 1994). Although these dolerites are relatively common throughout the Armorican Massif (Fig. 1), their ages are poorly constrained, due in particular to the difficulty to date this type of rock (Ruffet et al. 1992). Only one doubtful whole-rock K-Ar age of 330 ± 10 Ma (Perroud et al. 1986) is so far available. Because post-Devonian dikes are not observed in the field and because doleritic fragments have been observed inside early Carboniferous volcanic breccias and conglomerate (Plaine 1976), an age of around 360 Ma has been suggested for the emplacement of these mafic intrusions (Le Gall, 1999).

Description of the samples

Samples were collected within the un-metamorphosed North Armorican domain and the low-grade Central Armorican domain (Fig. 1): two within the Saint Malo group (MED1 and Vi1); three within the Laval Basin group (two in the southern part (PER1 and FOS9) and one in the northern part (SDO1)); one within the Mancellia group (MGX1); and one from the Martigné-Ferchaud group (MF1). Samples collected in the Saint Malo and Mancellia groups are very similar and consist of dolerite dikes intrusive within the Neoproterozoic basement (Fig. 1 and 2a). In the Laval Basin, two samples (PER1 and SDO1) consist of sills of dolerite intrusive within Silurian black shales (Fig. 2b), and a third sample (FOS 9) consists of an altered sill of dolerite found within Ordovician sandstones (Fig. 2c). In the Martigné-Ferchaud group, the sample belongs to a dolerite dike crosscutting Ordovician slates and sandstones and was subsequently partially hydrothermalized during the formation of Sb mineralization (Fig. 2d).

Despite their relatively wide geographical distribution, dolerites show similar textures and mineralogy. Only the mafic sill FOS9 is different from the others because it contains cm-scale phenocrysts of plagioclase that are strongly saussuritized and because it's magmatic texture is not preserved. The textures of the other doleritic samples are mainly porphyritic and the principal mineral assemblages consist of elongate plagioclase laths, clinopyroxene (mainly augite), and Fe-Ti oxides such as ilmenite, rutile, and magnetite with exsolved ilmenite (Fig. 3a). Late stage crystallization is represented by rare interstitial quartz (Fig. 3b, c and d) and/or quartz and alkali-feldspar intergrowths (granophyric textures). The accessory mineral assemblage consists of apatite, rare primary biotite and titanite, pyrite, chalcopyrite, pyrrhotite, chlorite, green amphibole, and epidote (pistachite). Apatite is the most common of all the accessory minerals and occurs in the groundmass of primary plagioclases but also in the mesostasis or within other minerals such as quartz, amphibole, or clinopyroxene (Fig. 3a, b, c and d). Apatite appears as euhedral and often acicular crystals up to 250 μm in length. Chemical weathering and hydrothermal alteration of these Armorican dolerites are common and may be locally strong. It is evidenced by the presence of sheets of silicates in interstitial glass, the destabilization of biotite into chlorite, and the replacement of clinopyroxene and plagioclase by a typical propylitic assemblage of chlorite, actinote, epidote, and carbonates.

Materials and methods

Major and trace elements analyses

Seven samples were collected mainly in quarries providing relatively fresh outcrop conditions. Only the least altered rocks were finally selected for analyses. These selected samples were crushed and powdered using agate mortars. Major and trace elements analyses, including REE,

were performed by the French analytical laboratory (SARM, CRPG-CNRS, Nancy) using an inductively coupled plasma optical emission spectrometry (ICP-OES) and mass spectrometry (ICP-MS), respectively, following the standard analytical procedures of Carignan et al (2001).

Mineral compositions

Apatite crystals were examined in polished thin-sections through a scanning electron microscope (SEM equipped with EDS), and analyzed using an electron microprobe (Cameca SXFive – Common analytical laboratory, BRGM-CNRS-University, Orléans, France). The major elements Ca, P, and F as well as Cl, Fe, Mg, Si, Mn, Sr, Na, and S were analyzed in the apatite crystals. It has been demonstrated that the measured X-ray flux from apatite is affected by crystal orientation (Stormer et al. 1993), nevertheless, highly accurate analyses of F and Cl can be achieved using low electron beam densities, large beams, and by analyzing grains with the electron beam perpendicular to the apatite c axis (Goldoff et al. 2012). Analyses were performed using a 15 kV accelerating voltage, a counting time of 10s, and a beam current of 6 nA for spot analyses, and 20nA for elemental mapping purposes, using the following mineral standards: Apatite (P Kα), Topaz (F Kα), Hematite (Fe Kα), Andradite (Ca Kα, Mg Kα), $MnTiO_3$ (Ti Kα), Celestite (Sr Kα, S Kα), Albite (Na Kα, Si Kα), and Vanadinite (Cl Kα). All the analyses were performed unambiguously with the electron beam perpendicular to the apatite c axis because of the strongly elongate shape of the grains. Several apatite grains were analysed per sample. The OH contents of apatite have been estimated from EPMA measurements of F and Cl by charge balance, assuming that the halogen sites are full (Piccoli and Candela 2002).

U-Pb analyses

Mineral separation procedures were applied to concentrate the apatite crystals using the facilities available at Géosciences Rennes. Rocks were crushed and only the powder fraction with a

239 diameter < 250 µm has been kept. Heavy minerals were successively concentrated using the
240 Wilfley table and heavy liquids. Magnetic minerals were then removed with an isodynamic
241 Frantz separator. Apatite grains were carefully handpicked under a binocular microscope and
242 embedded in epoxy mounts. The grains were then grounded and polished on a lap wheel with a 6
243 µm and 1 µm diamond suspension successively. Apatite grains were imaged by
244 cathodoluminescence (CL) using a Reliotron CL system equipped with a digital color camera
245 available in Géosciences Rennes.

246 U-Pb geochronology was conducted by in-situ laser ablation inductively coupled plasma
247 mass spectrometry (LA-ICPMS) at Géosciences Rennes using a ESI NWR193UC excimer laser
248 coupled to a quadripole Agilent 7700x ICP-MS equipped with a dual pumping system to enhance
249 sensitivity (Paquette et al. 2014). The instrumental conditions are reported in Table 1.
250 The ablated material is carried by He, which is then mixed with N_2 and Ar, before injection into
251 the plasma source. The alignment of the instrument and mass calibration was performed before
252 each analytical session on the NIST SRM 612 reference glass, by inspecting the ^{238}U signal and
253 by minimizing the ThO+/Th+ ratio (<0.5%). During the course of an analysis, the signals of ^{43}Ca,
254 $^{204}(Pb+Hg)$, ^{206}Pb, ^{207}Pb, ^{208}Pb, and ^{238}U masses are acquired. The ^{235}U signal is calculated from
255 ^{238}U on the basis of the ratio $^{238}U/^{235}U=137.88$.

256 Single analyses consisted of 20 s background integration followed by 60s integration with
257 the laser firing and then a 10 s delay to wash out the previous sample. Ablation spot diameters of
258 50 µm with repetition rates of 5 Hz were used for most of the samples. In some samples,
259 however, the apatite grains were acicular and could not therefore accommodate a 50 µm spot.
260 The ESI NWR193UC laser is equipped with a rotational XY shutter allowing to perform
261 rectangular ablations while ensuring an even "dosage" of the laser energy to the sample during
262 the analyses. In these cases, we defined a rectangle that was suitable for most of the grains from a

given sample. This ablation rectangle, which can rotate freely around its center, was then used for all the standards and the apatite crystals in order to use the same analytical conditions during the analyses.

For each sample (one analytical session of 43 measurements), we used the following standard bracketing procedure. Two analyses of the Madagascar apatite standard (ID-TIMS age of 473.5 ± 0.7 Ma; Cochrane et al. 2014) used as the primary apatite reference material, one analysis of the Durango apatite standard (31.44 ± 0.18 Ma; McDowell et al. 2005), one analysis of the McClure apatite standard (523.51 ± 2.09 Ma; Schoene and Bowring 2006), followed by 6 analyses of the apatite grains. This sequence was then repeated 3 times with one analysis of the Durango and two analyses of the Madagascar standards at the end of the session.

Data were corrected for U–Pb fractionation and for mass bias by the repeated measurements of the Madagascar apatite standard. The Durango and McClure apatite standards measurements were treated as unknowns and used to control the reproducibility and accuracy of the corrections. During the course of the analyses, they provided ^{207}Pb corrected ages of 32.22 ± 0.52 Ma (MSWD = 0.69; probability = 0.93) and 526.4 ± 3.3 Ma (MSWD = 0.57; probability = 0.98) respectively (Fig. 4a and b respectively).

Data reduction was carried out using the data reduction scheme VizualAge_UcomPbine, a set of Igor Pro procedures that work with Iolite (Chew et al. 2014). This data reduction scheme performs a common Pb correction using the ^{207}Pb method for the initial Pb isotope composition specified in the standard reference value file for the Madagascar apatite standard. Basically, a model downhole ^{207}Pb/^{235}U fractionation curve is fitted with a ^{207}Pb-based common Pb correction using an initial ^{207}Pb/^{206}Pb value of 0.8681 (Cochrane et al. 2014).

Whole-rock geochemistry

To account for the degree of alkali-element mobility during hydrothermal alteration or metasomatism, all the samples are plotted (Fig. 5a) in the $K_2O + Na_2O$ vs $K_2O/(K_2O + Na_2O)$ diagram of Hughes (1973). Most of the samples lie within the igneous spectrum field, with only two samples (FOS9) and a sample from the Mancellia group analyzed by Le Gall (1999) plotting outside of this field. This suggests that most of the mobile elements have not been significantly affected after the magma emplacement. For the Laval Basin group, samples are slightly altered with a loss of K_2O in some samples and almost a total loss of Na_2O in one sample (FOS9). According to the Zr/TiO_2 vs Nb/Y plot (Fig. 5b), most of the samples display basaltic affinities ($Zr/TiO_2 < 0.02$) with sub-alkalic ratios for the Saint-Malo group and the Martigné-Ferchaud (MF1) dike ($Nb/Y < 0.8$) and with sub-alkali to alkali ratios for the Mancellia and the Laval Basin groups ($0.4 > Nb/Y < 1.6$). Only one sample from the Mancellia group (MGX1) displays an intermediate affinity. Most of the samples have a relatively low MgO content (MgO < 6 wt%) except for PER1 (Table 2).

Data from this study, as well as the available values for different group of dolerites (Lahaye et al. 1995; Le Gall 1999), have been plotted in a chondrite-normalized spider diagram (Fig. 5c). Most of the dolerites display similar REE contents and sub-parallel REE patterns with a slight to moderate fractionation of the light REE vs. the heavy REE [$(La/Lu)_N$ = 3.56-7.45]. These patterns are similar to those reported for the Armorican dolerites by Le Gall (1999). Only sample FOS9 yields a moderate negative Eu anomaly. Although this sample is strongly altered (Fig. 5a), it shows a similar REE spectrum suggesting that the REE were not affected by hydrothermal alteration and/or chemical weathering. The mantle-normalized spider diagram (Fig. 5d) displays similar incompatible element contents and ratios for all the samples, with the exception of several elements such as Th, Hf-Zr, and Ti. Indeed, samples SDO1 and FOS9 show

slightly positive anomalies in Th that may be linked to the fact that the dolerites have incorporated some country rocks during their emplacement. The Zr-Hf fractionations (Zr/Hf = 35.65-46.07) are very similar for all the samples. Their respective contents are relatively high in sample MGX1 because of the presence of zircons inherited from the country rocks during emplacement. Three samples display negative anomalies in Ti ($Ti/Ti^* = [Ti]_N/[Sm]_N+[Gd]_N$ = 0.11-0.30) compared to the mean pattern for the Mancellia, Saint-Malo, and Laval Basin groups. The largest negative anomaly is recorded in the dike MGX1 (Ti = 1.87 wt%). Finally, the diagram also shows a light positive Y anomaly in sample PER1. According to mantle-normalized trace element patterns proposed by Li et al. (2015), most of the samples are similar to average compositions of alkaline continental flood basalts (CFB).

Apatite chemistry

We studied between 50 and 100 apatite grains for each of the 7 samples. In the MF1 and SDO1 samples, apatite grains appear as squat prisms up to 100 µm in length. In the PER1, MED1, and Vi1 samples, apatite crystals have an elongate acicular shape up to 150 µm in length and a width of ~ 25 µm. Finally, there are two types of apatite in samples MGX1 and FOS9: elongate crystals with an acicular shape up to 250 µm in length and squat grains up to 150 µm.

SEM examinations, X-Ray maps (Fig. 6a, b, c and d), and electron microprobe data show that F is always present in amounts above 0.62 apfu (Table 4), which indicates that all the apatite crystals are fluorapatite. These fluorapatite crystals are unzoned or sometimes poorly zoned around the rim. Oscillatory zoning has never been observed and, where present, the zoning is mainly marked by differences in the Mg (0 to 0.04 apfu), Mn (0 to 0.07 apfu), and Fe (0 to 0.07 apfu) contents. X-Ray maps reveal that the edges are slightly enriched in Mg and Fe (Fig. 6b and d) but the reverse has also been observed (eg sample SDO1). Average composition, standard

334 deviation, maximum and minimum (Table 4), demonstrate that these fluorapatite grains have a
335 narrow range of compositions and do not contain Sr despite the fact that Sr is available (between
336 48-455 ppm) in these rocks (Table 3). In the ternary OH-Cl-F diagram (Fig. 6e), most of the
337 grains match the compositions of fluorapatite from typically ultramafic/mafic complexes.
338 According to the data of Webster and Piccoli (2015), these compositions are the most frequently
339 encountered independently from the host-rock origin (mafic, felsic, and hydrothermal systems).
340

341 **Feasibility of U-Pb dating of apatite in mafic dike/sill**

342 In order to evaluate the feasibility to use apatite U-Pb to date the emplacement age of mafic
343 rocks, we performed some calculations and models dealing with the time necessary to crystallize
344 and cool these mafic dikes and sills. Firstly, we aim at estimating the time necessary to
345 completely crystallize a mafic dike or sill according to its thickness (up to 200 m) and the host-
346 rock temperatures (100, 200 and 300°C). We used the 1D analytical solution of the Stefan
347 problem transposed to dike and/or sill crystallization (see Turcotte and Schubert 1982 and Fig.
348 7a). For doleritic dikes and sills, we assumed that their rock parameters are close to basaltic ones.
349 Noteworthy, the solution implies that solidified doleritic magma and host rocks have the same
350 physical properties (i.e thermal diffusivity and specific heat capacity are similar for both
351 lithologies). The models show that the solidification can be considered as instantaneous (<20
352 years) on the geological time scale for a thickness less than 40 m whatever the host-rock
353 temperatures. When the mafic dikes or sills are thicker, the solidification times remain shorter
354 than 450 years. Consequently, the time necessary for the crystallization of the mafic dikes and
355 sills in this study is negligible.

356 Therefore, once solidified, we have to constrain the cooling temperature profile of a mafic
357 dike or sill in host rocks for different temperatures (100, 200, and 300 °C). At the end of the

358 solidification process, the temperature of the dolerite and its host rock has slightly changed when
359 compared to the solidus temperature (e.g. 1050 °C) and the initial host rock temperature.
360 However, in the following model, we consider that those changes are not significant considering
361 the thickness of the mafic dikes and sills sampled in this study. Therefore, we assume a
362 temperature of 1050 °C at the center of the dike or sill for t=0 (Fig. 7b). Models are built with a
363 2D finite element code using Comsol Multiphysics TM software in order to account for the
364 different physical properties between the dolerites and their host rocks, which is not possible with
365 the classical analytical 1D solution. We also calculated the apatite closure temperatures using the
366 Dodson (1973)'s equation with data from Cherniak et al. (1991). We used a radius ranging from
367 10 to 50 μm and the slowest cooling rate estimated for these dikes (7°C/year, Fig. 7b)
368 corresponding to a 60 m wide mafic sill or dike and a host rock temperature of 300°C. The
369 closure temperature obtained following these calculations range from 770 °C to 870 °C,
370 depending on the apatite radius. They are therefore well above the accepted closure range
371 between 375°C and 550°C because of the very fast cooling rate experienced by our samples.
372 Independent of the host rock temperature, the models show that time range for solidification of a
373 mafic dike or sill less than 60 m thick (maximum thickness of these intrusives) is very rapid (< 40
374 years). For a doleritic sill such as sample SDO1 (Fig. 1) with a thickness of ca. 60 m, the closure
375 temperature of apatite during post-solidification cooling is reached in less than 20 years.
376 Consequently, apatite appears to be a suitable mineral to date the emplacement age of such small-
377 size mafic bodies that have not been reheated above the closure temperature of apatite.

378 **Apatite dating**

379 We present the results obtained by U-Pb LA-ICP-MS dating on some of the apatite grains
380 described in the previous sections. For all the samples, the results are plotted in Tera-Wasserburg
381 diagrams using Isoplot/Ex (Ludwig 2012). All errors, given in Table S1 (supplementary data) and

the final results in Figures 8 and 9, are provided at 2σ level. In all the diagrams, the red dashed-lines represent the unforced discordias, and the black lines represent the discordias calculated if the initial common Pb value is forced to a $^{207}Pb/^{206}Pb$ value of 0.860 calculated following the Pb evolution model of Stacey and Kramers (1975) for an age of 360 Ma.

In the Saint-Malo group, data obtained from samples MED1 (dolerite dike) and Vi1 (dolerite dike) are discordant with a relatively high proportion of common Pb ($^{207}Pb/^{206}Pb$ values between 0.17–0.37 and 0.25–0.49, respectively). For sample MED1, the data define a lower intercept date of 362 ± 13 Ma (MSWD = 1.4) with a $^{207}Pb/^{206}Pb$ initial value of 0.853 (Fig. 8a). If the discordia is forced to a value of 0.860, we obtain a similar date of 363.0 ± 4.9 Ma (MSWD = 1.3). For sample Vi1, the unforced lower intercept date is 353 ± 17 Ma (MSWD = 1.8, initial $^{207}Pb/^{206}Pb$ value = 0.81). If the discordia is forced to a $^{207}Pb/^{206}Pb$ value of 0.860, the resulting lower intercept date is equivalent within error at 367.2 ± 5.6 Ma (MSWD = 2.1). The weighted average ^{207}Pb-corrected dates (calculated using Stacey and Kramers (1975) terrestrial Pb evolution model) are equivalent within error at 361.2 ± 6.3 Ma (MSWD = 0.62) for MED1 (Fig. 8c) and 363.9 ± 5.2 Ma (MSWD = 1.5) for Vi1 (Fig. 8d). The analyses of sample MF1 (dolerite dike in Martigné-Ferchaud locality) are also discordant with $^{207}Pb/^{206}Pb$ values between 0.25 – 0.32 (Fig. 8e). The unforced discordia date is 346 ± 17 Ma (MSWD = 2.2, initial $^{207}Pb/^{206}Pb$ value of 0.774). If we calculate the lower intercept date by forcing the discordia to a $^{207}Pb/^{206}Pb$ initial value of 0.860, we end up with a more precise date, comparable within error, at 363.3 ± 3.1 Ma (MSWD = 2.6). The weighted average ^{207}Pb-corrected date is 364 ± 14 Ma (MSWD = 0.041; Fig. 8f).

The analyses of MGX1 (dolerite dike from the Mancellia group) are discordant with various amounts of common Pb ($^{207}Pb/^{206}Pb$ values between 0.25-0.55). They provide a lower intercept date of 364.5 ± 9.7 Ma (MSWD = 0.39; $^{207}Pb/^{206}Pb$ = 0,837; Fig. 8g). When the

406 discordia is calculated with an initial $^{207}Pb/^{206}Pb$ value of 0.860, the resulting lower intercept date
407 is similar within error at 361.9 ± 4.2 Ma (MSWD = 0.39). The weighted average ^{207}Pb-corrected
408 date is equivalent within error at 369.7 ± 6.3 Ma (MSWD = 0.101; Fig. 8h).

409 In the Laval Basin group, the analyses of FOS9 (intermediate volcanic rock), SDO1 (sill
410 of dolerite), and PER1 (sill of dolerite) are also discordant with variable amounts of common Pb.
411 For samples FOS9 and SDO1, the amount of common Pb is high ($^{207}Pb/^{206}Pb$ values between
412 0.50–0.77 and 0.48–0.57). The lower intercept dates are constrained at 376 ± 12 Ma (MSWD =
413 2.0; $^{207}Pb/^{206}Pb$ initial value of 0.877) and 344 ± 44 Ma (MSWD = 3.0; $^{207}Pb/^{206}Pb$ initial value of
414 0.83), respectively (Fig. 9a and b). If the discordias are forced to a $^{207}Pb/^{206}Pb$ initial value of
415 0.860, the resulting lower intercept dates are 362.0 ± 3.9 (MSWD = 2.5) and 367.1 ± 6.7 Ma
416 (MSWD = 3.1), respectively, while the weighted average ^{207}Pb-corrected dates are similar at
417 362.6 ± 8.5 Ma (MSWD = 0.21; Fig. 9c) for FOS9 and 363.1 ± 6.7 Ma (MSWD = 1.3; Fig. 9d)
418 for SDO1. LA-ICPMS analyses of apatite grains from sample PER1 show the highest amount of
419 radiogenic Pb ($^{207}Pb/^{206}Pb$ = 0.14-0.29). The lower intercept date is at 354 ± 11 Ma (MSWD =
420 0.38; $^{207}Pb/^{206}Pb$ initial value of 0.81; Fig. 9e). If we calculate the lower intercept date by forcing
421 the discordia to a value of 0.860, we end up with a date comparable within error of 360.2 ± 3.8
422 Ma (MSWD =0.44). The weighted average ^{207}Pb-corrected date is 359.8 ± 4.3 Ma (MSWD =
423 0.27; Fig. 9f).
424

425 **Interpretation and discussion**

426 In the Northern and Central domains of the Armorican Massif, especially in the eastern part, the
427 regional metamorphism is of very low-grade with maximum temperatures close to 250-300°C
428 (Donnot et al. 1973; Le Corre 1969, 1975; Gloaguen et al. 2007). Consequently, we can assume
429 that the isotopic systems of the dated apatite grains were not reset after the emplacement of the

dikes. In all the samples, the crystals are not hydrothermal but primary and magmatic in origin because they are mainly found within magmatic plagioclase crystals.

In this study, the dolerite dikes are relatively thin with a maximum thickness of 10 m, whereas the dolerite sill is up to ~ 60 m thick in the Laval Basin. Because of their small thicknesses, numerical models show that the solidification and cooling of these mafic rocks was very fast (Fig. 7a and b). Therefore, although the apatite closure temperature is far cooler than the magma temperature, we can safely assume that the dates we obtain in this study can be interpreted as the emplacement ages for the mafic intrusives.

Furthermore, the apatite U-Pb dates obtained for the 7 samples are similar within error. In the case of the unforced discordias, the weighted average of the lower intercept dates is 360.3 ± 8.7 Ma (MSWD = 1.9), the ^{207}Pb-corrected mean date is 363.4 ± 5.8 Ma, and the weighted average of the lower intercept dates forced to a ^{207}Pb/^{206}Pb initial value of 0.860 is 363.0 ± 1.7 Ma (MSWD = 1.05). Even the most altered samples collected in the Laval Basin (PER1 and FOS9, Fig. 5a) yield a comparable age suggesting that the apatite U-Pb system is not necessarily disturbed when the rocks suffered some degree of hydrothermal alteration and weathering. Therefore, we conclude that all these samples were emplaced ca. 360 Ma ago. The ^{40}Ar/^{39}Ar dating of saussuritized plagioclase in a doleritic dike from the North Armorican domain give anomalous dates (330 ± 10 Ma) because of the presence of excess argon (Ruffet et al. 1992). Whereas apatite grains extracted from saussuritized plagioclase were not affected. This demonstrates that apatite should be considered as the best mineral to date mafic dike and sill emplacements even though they underwent propylitic alteration and very low-grade metamorphism. Nevertheless, further studies are necessary to unravel precisely the action of hydrothermal alteration and corrosive hot fluids on the apatite U-Pb geochronometer.

On the scale of our studied area (~160 x 200 km), within the Armorican Massif, we demonstrate that a major mafic magmatic event took place ca. 360 Ma ago, at least in the eastern part of the area. This age is confirmed by field evidence as doleritic fragments of the same nature are found within early Carboniferous volcanic breccias and conglomerates (Plaine 1976), and because dikes in post-Devonian rocks have never been observed (Le Gall 1999). This mafic magmatic event, characterized by geochemically homogeneous compositions with no significant crustal input, is interpreted as a within-plate type like alkaline continental flood basalts (Fig. 5d). It occurred on a regional scale during a brief episode and appears to be equivalent to the mafic and felsic volcanosedimentary sequences of the Châteaulin Basin in the western part of the Armorican Massif (Pelhate 1994; Caroff et al. 1996). This similarity seems to indicate that this major magmatic event can be generalized to the entire North and Central Armorican domains (ca. 40-45000 km²). This event appears coeval with a drastic change in the tectono-sedimentary regime. Indeed, it coincides with the paroxysm of high pressure, low temperature metamorphism recorded in the South Armorican domain (eclogite-facies in Champtoceaux complex, Bosse et al. 2000 and blueschist-facies in the Groix Island, Bosse et al. 2005) that marks the maximum depth of the presently exposed rocks from the north Gondwanian margin. At the same time, the distributed marine sedimentation becomes localized in the narrow Carboniferous basins (Fig. 1), such as the Laval or Châteaulin Basins, where continental sedimentary deposits occur locally. This period corresponds to the initiation of the collision sensu stricto of the Variscan orogeny in the Armorican Massif (Ballèvre et al. 2014). The origin of this magmatism may result from a melting of enriched lithospheric mantle (see the enrichment of LREE vs. HREE, Fig. 5c). However, additional geochemical investigations (e.g. radiogenic isotopes) are necessary to identify and characterize the geodynamical context and the deep sources responsible for this major mafic magmatic event.

Implications

Mafic rocks are generally difficult to date due to a lack of suitable minerals. Consequently, the dating of apatite by U-Pb LA-ICP-MS appears to be a very useful, quick, and pertinent method to date mafic rocks, which were emplaced in a single injection as dikes or sills. Furthermore, it is now evident that in-situ LA-ICP-MS dating, which is a fast and relatively inexpensive technique, can be successfully applied. We can, however, consider that this dating approach may not be suitable to date the emplacement age of large-scale layered mafic/ultramafic complexes or intrusions characterized by repeated injection of magma. However, it might be convenient to perform modelling of other examples of solidification and cooling in order to check the range of sizes and emplacement contexts for mafic intrusions that could be successfully dated using the U-Pb geochronometer on apatite. Prior to applying this dating technique, it is necessary to study the regional geology, especially the metamorphic, hydrothermal alteration, and/or weathering events that may have modified the chemistry and mineralogy of the studied rocks after their emplacement. Because of the relatively good precision (ca. 5 Ma) obtained in the age determination of the Variscan mafic rocks in this study, U-Pb LA-ICPMS geochronometry of apatite appears to be a key mineral in unraveling the history of mafic magmatism.

Acknowledgements

This work was supported by the French Geological Survey (BRGM), the region of Brittany, the OSUR,the CNRS-INSU and the Ulysses program (PHC). The authors thank the following groups and chief-geologists for allowing access to their granulate quarries: Y. Lemaitre and R. Le Droff from the “Pigeon Carrière” group, L. Seguin from the Eurovia group, the employees from the Hervé group, and the Nivet group. G. Wille (BRGM) is acknowledged for the microprobe

501 analytical analyses. We particularly thank X. Le Coz and Y. Lepagnot from Géosciences Rennes
502 laboratory for the thin sections and rock crushing preparations, respectively. We also address our
503 thanks to the SARM (Nancy) for the whole-rock geochemistry. Constructive reviews by D.
504 Chew, D. Harlov, and an anonymous reviewer have greatly improved the manuscript.
505
506
507
508

References cited

Aïfa, T., Lefort, J.-P., and Guennoc, P. (1999) Anisotropy of magnetic susceptibility investigations of the St Malo dyke swarm (Brittany, France): emplacement mechanism of doleritic intrusions. Geophysical Journal International, 139, 573–582.

Aldrich, L.T., Tilton, G.R., Davis, G.L., Nicolaysen, L.O., and Patterson, C.C. (1955) Comparison of U–Pb, Pb–Pb, and Rb–Sr ages of Precambrian minerals. In D.R. Derry, Ed., Symposium on Precambrian Correlation and Dating 7 pp. 7–13. Geological Association of Canada Proceedings.

Ballèvre, M., Bosse, V., Ducassou, C., and Pitra, P. (2009) Paleozoic history of the Armorican Massif: Models for the tectonic evolution of the suture zones. Comptes Rendus Geosciences, 341, 174–201.

Ballèvre, M., Catalán, J.R.M., López-Carmona, A., Pitra, P., Abati, J., Fernández, R.D., Ducassou, C., Arenas, R., Bosse, V., Castiñeiras, P., and others (2014) Correlation of the nappe stack in the Ibero-Armorican arc across the Bay of Biscay: a joint French–Spanish project. Geological Society, London, Special Publications, 405, 77–113.

Ballouard, C., Boulvais, P., Poujol, M., Gapais, D., Yamato, P., Tartèse, R., and Cuney, M. (2015) Tectonic record, magmatic history and hydrothermal alteration in the Hercynian Guérande leucogranite, Armorican Massif, France. Lithos, 220–223, 1–22.

Bosse, V., Féraud, G., Ruffet, G., Ballèvre, M., Peucat, J.-J., and De Jong, K. (2000) Late Devonian subduction and early-orogenic exhumation of eclogite-facies rocks from the Champtoceaux Complex (Variscan belt, France). Geological Journal, 35, 297–325.

Bosse, V., Féraud, G., Ballèvre, M., Peucat, J.-J., and Corsini, M. (2005) Rb–Sr and 40Ar/39Ar ages in blueschists from the Ile de Groix (Armorican Massif, France): Implications for closure mechanisms in isotopic systems. Chemical Geology, 220, 21–45.

533 Boudreau, A. (1995) Fluid evolution in layered intrusions: evidence from the chemistry of the
534 halogen-bearing minerals. In J.F.H. Thompson, Ed., Magmas, Fluids and Ore Deposits Vol. 23,
535 pp. 25–46. Geological Society of Canada Short Course.
536 Brun, J.-P., Guennoc, P., Truffert, C., and Vairon, J. (2001) Cadomian tectonics in northern
537 Brittany: a contribution of 3-D crustal-scale modelling. Tectonophysics, 331, 229–246.
538 Capdevila, R. (2010) Les granites variques du Massif Armoricain. Bulletin de la Société
539 géologique et minéralogique de Bretagne, (D) 7, 1–52.
540 Carignan, J., Hild, P., Mevelle, G., Morel, J., and Yeghicheyan, D. (2001) Routine Analyses of
541 Trace Elements in Geological Samples using Flow Injection and Low Pressure On-Line Liquid
542 Chromatography Coupled to ICP-MS: A Study of Geochemical Reference Materials BR, DR-N,
543 UB-N, AN-G and GH. Geostandards Newsletter, 25, 187–198.
544 Caroff, M., Le Gal, X., Rolet, J., Cotten, J., and Thonon, P. (1996) Magmatisme tholeiitique
545 continental en contexte orogénique hercynien□: l'exemple du volcanisme viséen de Kerroc'h,
546 Massif Armoricain (France). Comptes rendus de l'Académie des sciences de Paris, II, 322, 269–
547 275.
548 Carrapa, B., DeCelles, P.G., Reiners, P.W., Gehrels, G.E., and Sudo, M. (2009) Apatite triple
549 dating and white mica 40Ar/39Ar thermochronology of syntectonic detritus in the Central Andes:
550 A multiphase tectonothermal history. Geology, 37, 407–410.
551 Chamberlain, K.R., and Bowring, S.A. (2001) Apatite–feldspar U–Pb thermochronometer: a
552 reliable, mid-range (~450°C), diffusion-controlled system. Chemical Geology, 172, 173–200.
553 Chauris, L., Houlgatte, E., Laforêt, C., and Picot, P. (1985) Un district antimono-aurifère à
554 gangue quartzo-carbonatée□: Le Semnon (Ille-et-Vilaine, Massif Armoricain, France).
555 Hercynica, 1, 111–119.

556 Cherniak, D.J., Lanford, W.A., and Ryerson, F.J. (1991) Lead diffusion in apatite and zircon
557 using ion implantation and Rutherford Backscattering techniques. Geochimica et Cosmochimica
558 Acta, 55, 1663–1673.
559 Chew, D.M., Sylvester, P.J., and Tubrett, M.N. (2011) U–Pb and Th–Pb dating of apatite by LA-
560 ICPMS. Chemical Geology, 280, 200–216.
561 Chew, D.M., Petrus, J.A., and Kamber, B.S. (2014) U–Pb LA–ICPMS dating using accessory
562 mineral standards with variable common Pb. Chemical Geology, 363, 185–199.
563 Cochrane, R., Spikings, R.A., Chew, D., Wotzlaw, J.-F., Chiaradia, M., Tyrrell, S., Schaltegger,
564 U., and Van der Lelij, R. (2014) High temperature (>350 °C) thermochronology and mechanisms
565 of Pb loss in apatite. Geochimica et Cosmochimica Acta, 127, 39–56.
566 Cuney, M., Stussi, J.-M., Brouand, M., Dautel, D., Michard, A., Gros, Y., Poncet, D., Bouton, P.,
567 Colchen, M., and Vervialle, J.-P. (1993) Géochimie et géochronologie U/Pb des diorites
568 quartziques du Tallud et de Moncoutant: nouveaux arguments pour une extension de la “Ligne
569 Tonalitique Limousine” en Vendée. Comptes Rendus de l’Académie des Sciences de Paris, II,
570 316, 1383–1390.
571 Dodson, M.H. (1973) Closure temperature in cooling geochronological and petrological systems.
572 Contributions to Mineralogy and Petrology, 40, 259–274.
573 Donnot, M., Guigues, J., Lulzac, Y., Magnien, A., Parfenoff, A., and Picot, P. (1973) Un nouveau
574 type de gisement d’europium: la monazite grise à europium en nodules dans les schistes
575 paléozoïques de Bretagne. Mineralium Deposita, 8, 7–18.
576 Faure, G., and Mensing, T.M. (2005) Isotopes: principles and applications, xxvii+897 p. Wiley,
577 Hoboken, N.J., Etats-Unis d’Amérique.
578 Gapais, D., Lagarde, J.L., Le Corre, C., Audren, C., Jégouzo, P., Casas Sainz, A., and Van Den
579 Driessche, J. (1993) La zone de cisaillement de Quiberon : témoin d’extension de la chaine

580 varisque en Bretagne méridionale au Carbonifère. Comptes Rendus de l'Académie des Sciences
581 de Paris, II, 316, 1123–1129.
582 Gapais, D., Brun, J.-P., Gumiaux, C., Cagnard, F., Ruffet, G., and Veslud, C.L.C.D. (2015)
583 Extensional tectonics in the Hercynian Armorican belt (France). An overview. Bulletin de la
584 Société Géologique de France, 186, 117–129.
585 Gloaguen, E., Branquet, Y., Boulvais, P., Moelo, Y., Chauvel, J.-J., Chiappero, P.-J., and
586 Marcoux, E. (2007) Palaeozoic oolitic ironstone of the French Armorican Massif: a chemical and
587 structural trap for orogenic base metal–As–Sb–Au mineralisation during Hercynian strike-slip
588 deformation. Mineralium Deposita, 42, 399–422.
589 Goldoff, B., Webster, J.D., and Harlov, D.E. (2012) Characterization of fluor-chlorapatites by
590 electron probe microanalysis with a focus on time-dependent intensity variation of halogens.
591 American Mineralogist, 97, 1103–1115.
592 Green, T.H., and Watson, E.B. (1982) Crystallization of apatite in natural magmas under high
593 pressure, hydrous conditions, with particular reference to "Orogenic" rock series. Contributions
594 to Mineralogy and Petrology, 79, 96–105.
595 Gumiaux, C., Brun, J.P., and Gapais, D. (2004a) Strain removal within the Hercynian Shear Belt
596 of Central Brittany (western France): methodology and tectonic implications. Geological Society,
597 London, Special Publications, 224, 287–305.
598 Gumiaux, C., Gapais, D., Brun, J.P., Chantraine, J., and Ruffet, G. (2004b) Tectonic history of
599 the Hercynian Armorican Shear belt (Brittany, France). Geodinamica Acta, 17, 289–307.
600 Harrison, T.M., and Watson, E.B. (1984) The behavior of apatite during crustal anatexis:
601 Equilibrium and kinetic considerations. Geochimica et Cosmochimica Acta, 48, 1467–1477.
602 Harrison, T.M., Catlos, E.J., and Montel, J.-M. (2002) U-Th-Pb Dating of Phosphate Minerals.
603 Reviews in Mineralogy and Geochemistry, 48, 524–558.

Houlgatte, E., Le Hérissé, A., Pelhate, A., and Rolet, J. (1988) Evolution géodynamique du bassin carbonifère de Laval (Massif Armoricain). Géologie de la France, n°1, 27–46.

Hughes, C.J. (1973) Spilites, keratophyres and the igneous spectrum. Geological Magazine, 503–527.

Hughes, J.M., and Rakovan, J. (2002) The Crystal Structure of Apatite, Ca5(PO4)3(F,OH,Cl). Reviews in Mineralogy and Geochemistry, 48, 1–12.

Kelley, S. (2002) Excess argon in K–Ar and Ar–Ar geochronology. Chemical Geology, 188, 1–22.

Lahaye, Y., Blais, S., Auvray, B., and Ruffet, G. (1995) Le Volcanisme fissural paleozoique du domaine nord-armoricain. Bulletin de la Societe Geologique de France, 166, 601–612.

Le Corre, C. (1969) Sur une paragenèse à chloritoïde dans les schistes de l'Ordovicien moyen des synclinaux du Sud de Rennes (Massif Armoricain). Bulletin de la Société Géologique Minéralogique de Bretagne, C, 33–44.

Le Corre, C. (1975) Analyse comparee de la cristallinite des micas dans le Brioverien et le Paleozoique centre-armoricains; zoneographie et structure d'un domaine epizonal. Bulletin de la Societe Geologique de France, 7, XVII, 547–553.

Le Gall, J. (1999) Les dolérites et basaltes tholéiitiques varisques du domaine nord-est armoricain. Géologie de la France, 4, 3–26.

Le Gall, J., and Mary, G. (1983) Place et signification du complexe basique de Brée et des autres venues gabbroïques et doléritiques dans l'histoire cadomo-varisque de l'Est du Massif Armoricain. Bulletin de la Société géologique et minéralogique de Bretagne, C-15, 169–180.

Li, C., Arndt, N.T., Tang, Q., and Ripley, E.M. (2015) Trace element indiscrimination diagrams. Lithos, 232, 76–83.

627 Ludwig, K.R. (2012) User's Manual for Isoplot 3.75. A geochronological toolkit for Microsoft
628 Excel. Berkeley Geochronological Cent, 1–75.
629 Mary, G., and Le Gall, J. (1985) Le Dinantien basal du flanc Nord du Bassin de Laval à
630 Argentré□: volcanites basiques et formations volcano-sédimentaires. Hercynica, 1, 155–163.
631 Matte, P. (1986) La chaîne Varisque parmi les chaînes Paléozoïques péri atlantiques, modèle
632 d'évolution et position des grands blocs continentaux au Permo-Carbonifère. Bulletin de la
633 Société Géologique de France, 8, II, 9–24.
634 McConnell, D. (1938) A structural investigation of the isomorphism of the apatite group.
635 American Mineralogist, 23, 1–19.
636 McDowell, F.W., McIntosh, W.C., and Farley, K.A. (2005) A precise 40Ar–39Ar reference age
637 for the Durango apatite (U–Th)/He and fission-track dating standard. Chemical Geology, 214,
638 249–263.
639 Oosthuyzen, E.J., and Burger, A.J. (1973) The suitability of apatite as an age indicator by the
640 uranium-lead isotope method. Earth and Planetary Science Letters, 18, 29–36.
641 Paquette, J.-L., Piro, J.L., Devidal, J.L., Bosse, V., Didier, A., Sanac, S., and Abdelnour, Y.
642 (2014) Sensitivity enhancement in LA-ICP-MS by N2 addition to carrier gas: Application to
643 radiometric dating of U-Th-bearing minerals. Agilent ICP-MS Journal, 58, 4–5.
644 Paton, C., Woodhead, J.D., Hellstrom, J.C., Hergt, J.M., Greig, A., and Maas, R. (2010)
645 Improved laser ablation U-Pb zircon geochronology through robust downhole fractionation
646 correction. Geochemistry, Geophysics, Geosystems, 11, Q0AA06.
647 Pearce, J.A. (1996) A user's guide to basalt discrimination diagrams. In D.A. Wyman, Ed., Trace
648 element geochemistry of volcanic rocks: applications for massive sulphide exploration. Vol. 12,
649 pp. 79–113. Geological Association of Canada, Short Course Notes.

650 Pelhate, A. (1994) Carboniferous of the Armorican Massif. In J. Chantraine, J. Rolet, D.S.
651 Santallier, A. Piqué, and J.D. Keppie, Eds., Pre-Mesozoic Geology in France and Related Areas
652 pp. 162–168. Springer Berlin Heidelberg.
653 Perroud, H., Auvray, B., Bonhommet, N., Mace, J., and Van Der Voo, R. (1986)
654 Palaeomagnetism and K-Ar dating of lower carboniferous dolerite dykes from northern Brittany.
655 Geophysical Journal of the Royal Astronomical Society, 87, 143–154.
656 Peucat, J.-J., Auvray, B., Hirbec, Y., and Calvez, J.-Y. (1984) Granites et cisaillements
657 hercyniens dans le Nord du Massif Armoricain; geochronologie Rb-Sr. Bulletin de la Societe
658 Geologique de France, 7, XXVI, 1365–1373.
659 Piccoli, P.M., and Candela, P.A. (2002) Apatite in Igneous Systems. Reviews in Mineralogy and
660 Geochemistry, 48, 255–292.
661 Plaine, J. (1976) La bordure sud du synclinorium Paléozoïque de Laval (Massif armoricain)□:
662 stratigraphie, volcanisme, structure. Université de Rennes, Rennes.
663 Pochon, A., Gapais, D., Gloaguen, E., Gumiaux, C., Branquet, Y., Cagnard, F., and Martelet, G.
664 (2016) Antimony deposits in the Variscan Armorican belt, a link with mafic intrusives? Terra
665 Nova, 28, 138–145.
666 Reiners, P.W., Ehlers, T.A., and Zeitler, P.K. (2005) Past, Present, and Future of
667 Thermochronology. Reviews in Mineralogy and Geochemistry, 58, 1–18.
668 Rolet, J., Gresselin, F., Jegouzo, P., Ledru, P., and Wyns, R. (1994) Intracontinental Hercynian
669 Events in the Armorican Massif. In J. Chantraine, J. Rolet, D.S. Santallier, A. Piqué, and J.D.
670 Keppie, Eds., Pre-Mesozoic Geology in France and Related Areas pp. 195–219. Springer Berlin
671 Heidelberg.
672 Ruffet, G., Perroud, H., and Féraud, G. (1992) Palaeomagnetism and 40Ar/39Ar dating of the
673 Trégor dolerites (Armorican Massif, France). Tectonophysics, 201, 121–140.

674 Schoene, B., and Bowring, S.A. (2006) U–Pb systematics of the McClure Mountain syenite:
675 thermochronological constraints on the age of the 40Ar/39Ar standard MMhb. Contributions to
676 Mineralogy and Petrology, 151, 615–630.
677 Schoene, B., and Bowring, S.A. (2007) Determining accurate temperature–time paths from U–Pb
678 thermochronology: An example from the Kaapvaal craton, southern Africa. Geochimica et
679 Cosmochimica Acta, 71, 165–185.
680 Spear, F.S., and Pyle, J.M. (2002) Apatite, Monazite, and Xenotime in Metamorphic Rocks.
681 Reviews in Mineralogy and Geochemistry, 48, 293–335.
682 Stacey, J.S., and Kramers, J.D. (1975) Approximation of terrestrial lead isotope evolution by a
683 two-stage model. Earth and Planetary Science Letters, 26, 207–221.
684 Storey, C.D., Smith, M.P., and Jeffries, T.E. (2007) In situ LA-ICP-MS U–Pb dating of
685 metavolcanics of Norrbotten, Sweden: Records of extended geological histories in complex
686 titanite grains. Chemical Geology, 240, 163–181.
687 Stormer, J.C., Pierson, M.L., and Tacker, R.C. (1993) Variation of F and Cl X-ray intensity due
688 to anisotropic diffusion in apatite during electron microprobe analysis. American Mineralogist,
689 78, 641–648.
690 Sun, S.S., and McDonough, W.F. (1989) Chemical and isotopic systematics of oceanic basalts:
691 implications for mantle composition and processes. Geological Society, London, Special
692 Publications, 42, 313–345.
693 Tartèse, R., and Boulvais, P. (2010) Differentiation of peraluminous leucogranites “en route” to
694 the surface. Lithos, 114, 353–368.
695 Tartèse, R., Boulvais, P., Poujol, M., and Vigneresse, J.-L. (2011a) Granite petrogenesis revealed
696 by combined gravimetric and radiometric imaging. Tectonophysics, 501, 98–103.

Tartèse, R., Poujol, M., Ruffet, G., Boulvais, P., Yamato, P., and Košler, J. (2011b) New U-Pb zircon and 40Ar/39Ar muscovite age constraints on the emplacement of the Lizio syn-tectonic granite (Armorican Massif, France). Comptes Rendus Geoscience, 343, 443–453.

Thomson, S.N., Gehrels, G.E., Ruiz, J., and Buchwaldt, R. (2012) Routine low-damage apatite U-Pb dating using laser ablation–multicollector–ICPMS. Geochemistry, Geophysics, Geosystems, 13, Q0AA21.

Tilton, G.R., Patterson, C., Brown, H., Inghram, M., Hayden, R., Hess, D., and Larsen, E. (1955) Isotopic Composition and Distribution of Lead, Uranium, and Thorium in a Precambrian Granite. Geological Society of America Bulletin, 66, 1131–1148.

Turcotte, D.L., and Schubert, G. (1982) Geodynamics: Applications of continuum physics to geological problems, 450 p. John Wiley & Sons, New-York.

Velde, D. (1970) Les filons doleritiques du Nord de la Bretagne. Bulletin de la Societe Geologique de France, 7, XII, 843–855.

Vidal, P. (1980) L'évolution polyorogénique du Massif armoricain; apport de la géochimie isotopique du strontium. Mémoires de la Société Géologique et Minéralogique de Bretagne, 21, 162p.

Watson, E.B. (1979) Apatite saturation in basic to intermediate magmas. Geophysical Research Letters, 6, 937–940.

Watson, E.B. (1980) Apatite and phosphorus in mantle source regions: An experimental study of apatite/melt equilibria at pressures to 25 kbar. Earth and Planetary Science Letters, 51, 322–335.

Webster, J.D., and Piccoli, P.M. (2015) Magmatic Apatite: A Powerful, Yet Deceptive, Mineral. Elements, 11, 177–182.

Whitney, D.L., and Evans, B.W. (2010) Abbreviations for names of rock-forming minerals. American mineralogist, 95, 185–187.

721 Winchester, J.A., and Floyd, P.A. (1977) Geochemical discrimination of different magma series
722 and their differentiation products using immobile elements. Chemical Geology, 20, 325–343.

723
724

725

726

List of figure captions

Figure 1: Simplified geological map of the Armorican Massif modified from Chantraine et al. (1996) and Le Gall (1999). P = Plouaret granite; G = Guérande granite; L = Lizio granite; Pl = Ploumanac'h granite. Sample names and locations are reported in the WGS84 geographic coordinate system: Vi1 (48°16'5.23"N, 1°45'20.03"W); MED1 (48°17'0.05"N, 1°40'1.67"W); MGX1 (48°12'52.26"N, 0°41'55.74"W); PER1 (47°59'22.98"N, 0°44'30.32"W); SDO1 (48°0'34.05"N, 0°17'53.39"W); FOS9 (47°56'17.62"N, 0°42'20.79"W); MF1 (47°50'26.83"N, 1°18'0.71"W).

Figure 2: Representative field photographs showing: (a) A typical dolerite dike intruding Neoproterozoic basement from the Saint-Malo group in the North Armorican domain. (b) A sill of dolerite intruding Silurian black shales in the northern part of the Laval Basin. The white dashed line represents the contact between the sill and the host rock. (c) A mafic intrusive facies with phenocrysts of plagioclase within Ordovician sandstones in the southern part of the Laval Basin. (d) A hydrothermalized dolerite dike associated with Sb mineralization in Ordovician slates from the Martigné-Ferchaud group.

Figure 3: Selected thin section micro-photographs illustrating: (a) the typical texture of a dolerite dike with laths of plagioclase intergrown with clinopyroxene and apatite crystals occurrence in the groundmass of fresh and saussuritized plagioclase and acicular apatite in clinopyroxene. (b) Primary amphibole and interstitial anhedral quartz (< 2 %) in dolerite dike. (c) Apatite growing in primary amphibole and interstitial quartz. (d) Several apatite crystals in the groundmass of plagioclase, interstitial quartz, and clinopyroxene. See Whitney and Evans (2010) for mineral abbreviations.

751

752 **Figure 4:** Diagrams representing the weighted average ^{207}Pb-corrected measured ages for the
753 secondary apatite standards analyzed during this study: (a) Durango apatite and (b) McClure
754 apatite. Prob. = Probability.

755

756 **Figure 5:** (a) Whole-rock composition in the chemical diagram of Hughes (1973) for the dolerite
757 samples. (b) Zr/TiO_2 vs. Nb/Y diagram of Winchester and Floyd (1977) modified by Pearce
758 (1996) with alkaline, subalkaline, basic, and intermediate rocks subdivision. (c) Chondrite
759 normalized REE diagram and (d) mantle-normalized spider diagrams reporting the mean patterns
760 for the Mancellia, Laval Basin and Saint-Malo groups of dolerite. Chondrite and primitive mantle
761 normalizing values are taken from Sun and McDonough (1989).

762

763 **Figure 6:** Chemistry of representative poorly-zoned fluorapatite crystals using X-ray maps: (a) P
764 Kα, (b) Fe Kα, (c) F Kα, and (d) Mg Kα. (e) plot of the halogen contents (in molar proportions)
765 with fields from various mafic layered intrusions modified after Boudreau (1995).

766

767 **Figure 7**: (a) Solidification time (time necessary for a complete crystallization of the magma) vs.
768 thickness of doleritic dikes and/or sills for three different host rock temperatures (100, 200, and
769 300 °C). Calculation was performed using a crystallization temperature of 1050 °C, a latent heat
770 of 400 $kJkg^{-1}$, a mean specific heat capacity of 1 $kJkg^{-1}K^{-1}$ and a mean thermal diffusivity of $7e^{-7}m^2s^{-1}$. (b) Cooling temperature of the center of a mafic dike/sill vs. time as a function of different
772 thicknesses and host rock temperatures. For a mafic rock density of 3000 kg m^{-3}, the specific heat
773 capacity is 800 $Jkg^{-1}K^{-1}$ and the thermal conductivity is 3.5 $Wm^{-1}K^{-1}$. Host rocks properties
774 correspond to averages for silico-clastic metasediments with a density of 2800 kg m^{-3}, specific

775 heat capacity of 750 $Jkg^{-1}K^{-1}$, and thermal conductivity of 2 $Wm^{-1}K^{-1}$. Colors used correspond to
776 a dike or a sill with a thickness of 1 m (orange), 10 m (blue), 20 m (black), and 60 m (red).
777
778 **Figure 8:** Tera-Wasserburg concordia diagram with the corresponding ^{207}Pb-corrected average
779 dates for the dolerites from the Saint-Malo group with samples MED1 and Vi1 (a, b, c, and d),
780 the Martigné-Ferchaud group with sample MF1 (e and f) and the Mancellia group with sample
781 MGX1 (g and h). The red dashed-lines represent the unforced discordias and the black lines
782 represent the discordias calculated if the initial common Pb value is forced to a $^{207}Pb/^{206}Pb$ value
783 of 0.860 calculated following the Pb evolution model of Stacey and Kramers (1975) for an age of
784 360 Ma. N corresponds to the number of apatite grains that have been analyzed per sample.
785 Ellipses and errors are reported at 2σ.
786
787 **Figure 9:** Tera-Wasserburg concordia diagram and the corresponding ^{207}Pb-corrected average
788 dates for dolerites from the Basin Laval for samples FOS9, SDO1 (a, b, c and d) and PER1 (e and
789 f). See legend in the Figure 8.
790

This is a preprint, the final version is subject to change, of the American Mineralogist (MSA)
Cite as Authors (Year) Title. American Mineralogist, in press.
(DOI will not work until issue is live.) DOI: http://dx.doi.org/10.2138/am-2016-5736

Table 1. Operating conditions for the LA-ICP-MS equipment

	U-Pb apatite analyses
Laboratory & Sample Preparation	
Laboratory name	Géosciences Rennes, UMR CNRS 6118, Rennes, France
Sample type/mineral	Magmatic apatite
Sample preparation	Conventional mineral separation, 1 inch resin mount, 1µm polish to finish
Imaging	CL: RELION CL instrument, Olympus Microscope BX51WI, Leica Color Camera DFC 420C
Laser ablation system	
Make, Model & type	ESI NWR193UC, Excimer
Ablation cell	ESI NWR TwoVol2
Laser wavelength	193 nm
Pulse width	< 5 ns
Fluence	6.5 J/cm-2
Repetition rate	5 Hz
Spot size	50 µm (round spot) or 70x30 µm (rotational XY shutter)
Sampling mode / pattern	Single spot
Carrier gas	100% He, Ar make-up gas and N2 (3 ml/mn) combined using in-house smoothing device
Background collection	20 seconds
Ablation duration	60 seconds
Wash-out delay	15 seconds
Cell carrier gas flow (He)	0.75 l/min
ICP-MS Instrument	
Make, Model & type	Agilent 7700x, Q-ICP-MS
Sample introduction	Via conventional tubing
RF power	1350W
Sampler, skimmer cones	Ni
Extraction lenses	X type
Make-up gas flow (Ar)	0.87 l/min
Detection system	Single collector secondary electron multiplier
Data acquisition protocol	Time-resolved analysis
Scanning mode	Peak hopping, one point per peak
Detector mode	Pulse counting, dead time correction applied, and analog mode when signal intensity > ~ 10^6 cps
Masses measured	^{43}Ca, ^{204}(Hg + Pb), ^{206}Pb, ^{207}Pb, ^{208}Pb, ^{232}Th, ^{238}U
Integration time per peak	10-30 ms
Sensitivity / Efficiency	28000 cps/ppm Pb (50µm, 10Hz)
Dwell time per isotope	5-70 ms depending on the masses
Data Processing	
Gas blank	20 seconds on-peak
Calibration strategy	Madagascar apatite used as primary reference material, Durango and McClure apatites used as secondary reference material (quality control)
Reference Material info	Madagascar (Thomson et al. 2012) Durango (McDowell et al. 2005) McClure (Schoene and Bowring 2006)
Data processing package used	Iolite (Paton et al. 2010), VizualAge_UcomPbine (Chew et al. 2014)
Quality control / Validation	Durango: Weighted average ^{207}Pb corrected age = 32.22 ± 0.52 Ma (MSWD = 0.69; probability=0.93) McClure: Weighted average ^{207}Pb corrected age = 526.4 ± 3.3 Ma (MSWD = 0.57; probability = 0.98)

This is a preprint, the final version is subject to change, of the American Mineralogist (MSA)
Cite as Authors (Year) Title. American Mineralogist, in press.
(DOI will not work until issue is live.) DOI: http://dx.doi.org/10.2138/am-2016-5736

Table 2. Major elements from studied rock samples.

Sample	MED1	Vi1	SDO1	PER1[a]	FOS9	MF1	MGX1
Facies	**Dolerite**	**Dolerite**	**Dolerite**	**Dolerite**	**Andesite**	**Dolerite**	**Dolerite**
SiO2	47.43	43.96	50.91	42.32	51.82	46.30	54.74
Al2O3	13.26	15.19	13.92	11.75	20.23	15.58	12.42
Fe2O3	14.413	15	12.707	12.86	12.40	14.24	14.05
MnO	0.20	0.20	0.15	0.11	0.18	0.19	0.26
MgO	5.51	5.95	3.43	11.15	3.53	5.99	2.00
CaO	9.22	7.53	6.63	6.04	0.64	7.58	5.31
Na2O	2.84	2.99	2.67	1.45	0.04	2.46	3.61
K2O	0.56	0.99	1.83	0.1	1.94	0.99	1.85
TiO2	3.56	3.38	3.10	2.58	1.81	2.81	1.87
P2O5	0.46	0.43	0.74	0.38	0.47	0.28	0.90
PF	1.35	3.50	2.95	11.6	8.22	2.84	2.05
Total	98.79	99.11	99.03	100.34	101.26	99.27	99.05

Notes: [a] The chemical composition of PER1 sample were performed by Le Gall (1999)

Table 3. Trace elements and REE from studied rock samples.

Sample	MED1	Vi1	SDO1	PER1	FOS9	MF1	MGX1
As	bdl	2.369	bdl	-	36.39	bdl	bdl
Ba	123.4	254.6	479.1	47	442.9	457.7	413.4
Be	1.54	1.609	2.326	-	6.587	1.169	3.339
Bi	bdl	bdl	bdl	-	bdl	bdl	bdl
Cd	0.286	0.233	0.421	-	0.411	0.296	1.499
Co	41.34	44.03	28.92	69	27.01	47.04	15.36
Cr	118.2	69.54	19.45	384	55.5	50	bdl
Cs	1.572	3.426	0.676	-	3.294	8.876	4.24
Cu	48.65	26.85	18.53	57	30.12	31.3	22.12
Ga	23.74	22.34	27.48	-	29.19	23.2	31.66
Ge	1.766	1.634	1.534	-	1.309	1.512	2.08
Hf	6.43	5.673	11.31	-	8.844	4.644	32.32
In	0.139	0.13	0.153	-	bdl	0.14	0.228
Mo	1.364	1.543	2.142	-	1.917	bdl	3.85
Nb	26.27	22.29	34.69	0	22.56	13.73	58.18
Ni	60.46	54.86	23.19	345	52.99	65.33	bdl
Pb	2.2269	1.9958	9.0967	-	9.4729	2.4961	8.926
Rb	13	43.54	41.94	bdl	58.25	56.89	42.94
Sc	32.34	24.09	21.03	0	23.48	28.24	28.8
Sb	bdl	0.251	bdl	-	4.723	bdl	bdl
Sn	2.96	2.536	3.331	-	3.446	2.302	6.048
Sr	307.9	318.6	281.1	222	48.66	455.1	234.1
Ta	2.087	1.716	2.638	-	1.746	1.114	4.166
Th	2.759	1.701	8.165	bdl	7.839	1.673	6.246
U	0.708	0.475	1.812	-	3.808	0.406	2.084
V	343.1	215.1	176.7	226	134.5	220.9	38.43
W	0.6	0.474	0.746	-	16.67	bdl	0.993
Y	37.32	34.47	50.66	25.17	55.81	32.81	89.84
Zn	142.4	132.7	165.9	bdl	195.8	161.9	251.4
Zr	267.6	239.4	403.2	bdl	351.6	166	1489
La	24.42	20.41	43.2	14.17	33.86	14.97	55.23
Ce	53.73	45.1	97.35	35.05	71.49	32.7	123.8
Pr	7.519	6.354	12.71	-	9.641	4.796	18.26
Nd	33.25	28.6	55.22	21.71	40.88	21.94	82.27
Sm	8.377	7.289	13.21	5.84	9.448	5.973	20.66
Eu	2.73	2.611	3.788	1.99	2.571	2.036	6.989
Gd	8.138	7.158	12	5.75	9.412	6.256	19.55
Tb	1.235	1.113	1.801	-	1.451	1.017	2.965
Dy	7.506	6.875	10.51	4.87	9.139	6.252	17.7
Ho	1.495	1.355	2.031	-	1.999	1.292	3.518
Er	3.682	3.364	5.012	2.03	5.272	3.282	8.922
Tm	0.484	0.46	0.646	-	0.742	0.442	1.216
Yb	3.191	3.014	4.245	1.76	4.982	2.886	7.943
Lu	0.451	0.435	0.602	0.26	0.776	0.436	1.217

Notes : bdl = below detection limit

This is a preprint, the final version is subject to change, of the American Mineralogist (MSA)
Cite as Authors (Year) Title. American Mineralogist, in press.
(DOI will not work until issue is live.) DOI: http://dx.doi.org/10.2138/am-2016-5736

Table 4. Average electron microprobe analyses and corresponding structural formulas of apatite

	APATITE													
Sample	MF1 (n=20)	σ	FOS9 (n=43)	σ	SDO1 (n=11)	σ	MED1 (n=23)	σ	Vi1 (n=10)	σ	MGX1 (n=17)	σ	PER1 (n=12)	σ
CaO	54.35	0.24	54.26	0.28	54.82	0.33	54.34	0.36	54.20	0.33	54.63	0.97	54.33	0.36
SrO	0.00	0.00	0.00	0.02	0.00	0.00	0.00	0.00	0.00	0.00	0.04	0.02	0.09	0.04
MgO	0.21	0.04	0.19	0.07	0.01	0.03	0.11	0.10	0.07	0.08	0.28	0.12	0.24	0.04
MnO	0.01	0.06	0.01	0.05	0.00	0.00	0.00	0.00	0.00	0.00	0.09	0.03	0.05	0.04
FeO	0.43	0.20	0.55	0.26	0.00	0.00	0.20	0.25	0.12	0.20	0.75	0.66	0.35	0.12
Na_2O	0.00	0.00	0.03	0.07	0.06	0.09	0.06	0.10	0.15	0.08	0.05	0.03	0.02	0.02
P_2O_5	40.96	0.25	41.62	0.24	41.32	0.27	41.37	0.37	41.34	0.14	41.63	0.79	40.86	0.44
SiO_2	0.63	0.12	0.14	0.07	0.23	0.05	0.47	0.21	0.33	0.11	0.31	0.39	0.58	0.14
SO_3	0.00	0.00	0.00	0.01	0.00	0.00	0.00	0.02	0.00	0.00	0.00	0.00	0.00	0.00
F	2.48	0.09	2.94	0.17	3.34	0.14	2.71	0.21	3.12	0.41	2.84	0.29	2.91	0.15
Cl	0.18	0.04	0.16	0.05	0.37	0.04	0.18	0.05	0.09	0.03	0.17	0.03	0.25	0.04
Total	99.25	0.28	99.91	0.38	100.15	0.50	99.45	0.41	99.42	0.39	100.78	0.81	99.68	0.62
O=F	1.04	0.04	1.24	0.07	1.40	0.06	1.14	0.09	1.32	0.17	1.20	0.12	1.23	0.06
O=Cl	0.04	0.01	0.04	0.01	0.08	0.01	0.04	0.01	0.02	0.01	0.04	0.01	0.06	0.01
Total*	98.16	0.29	98.64	0.36	98.67	0.49	98.26	0.39	98.09	0.29	99.54	0.78	98.40	0.59
Structural formula on the basis of a 12.5 oxygen equivalent														
Ca	4.95	0.02	4.93	0.03	5.00	0.02	4.95	0.04	4.95	0.03	4.92	0.05	4.96	0.03
Sr	0.00	0.00	0.00	0.00	0.00	0.00	0.00	0.00	0.00	0.00	0.00	0.00	0.00	0.00
Mg	0.03	0.01	0.02	0.01	0.00	0.00	0.01	0.01	0.01	0.01	0.04	0.02	0.03	0.00
Mn	0.00	0.02	0.04	0.00	0.00	0.00	0.00	0.00	0.00	0.00	0.02	0.01	0.01	0.01
Fe	0.03	0.01	0.04	0.02	0.00	0.00	0.01	0.02	0.01	0.01	0.05	0.05	0.02	0.01
Na	0.00	0.00	0.00	0.01	0.01	0.01	0.01	0.02	0.03	0.01	0.01	0.01	0.00	0.00
P	2.95	0.01	2.99	0.01	2.98	0.01	2.98	0.02	2.98	0.01	2.96	0.03	2.95	0.01
Si	0.05	0.01	0.01	0.01	0.02	0.00	0.04	0.02	0.03	0.01	0.03	0.03	0.05	0.01
S	0.00	0.00	0.00	0.00	0.00	0.00	0.00	0.00	0.00	0.00	0.00	0.00	0.00	0.00
F	0.67	0.02	0.79	0.05	0.90	0.04	0.73	0.06	0.84	0.11	0.76	0.08	0.78	0.04
Cl	0.03	0.01	0.02	0.01	0.05	0.01	0.03	0.01	0.01	0.00	0.02	0.00	0.04	0.01
OH[a]	0.30	0.03	0.19	0.05	0.05	0.04	0.24	0.05	0.15	0.11	0.22	0.08	0.18	0.04

Notes: Oxide contents in wt.%, cationic contents in apfu and σ: standard deviation

This is a preprint, the final version is subject to change, of the American Mineralogist (MSA)
Cite as Authors (Year) Title. American Mineralogist, in press.
(DOI will not work until issue is live.) DOI: http://dx.doi.org/10.2138/am-2016-5736

Figure 1

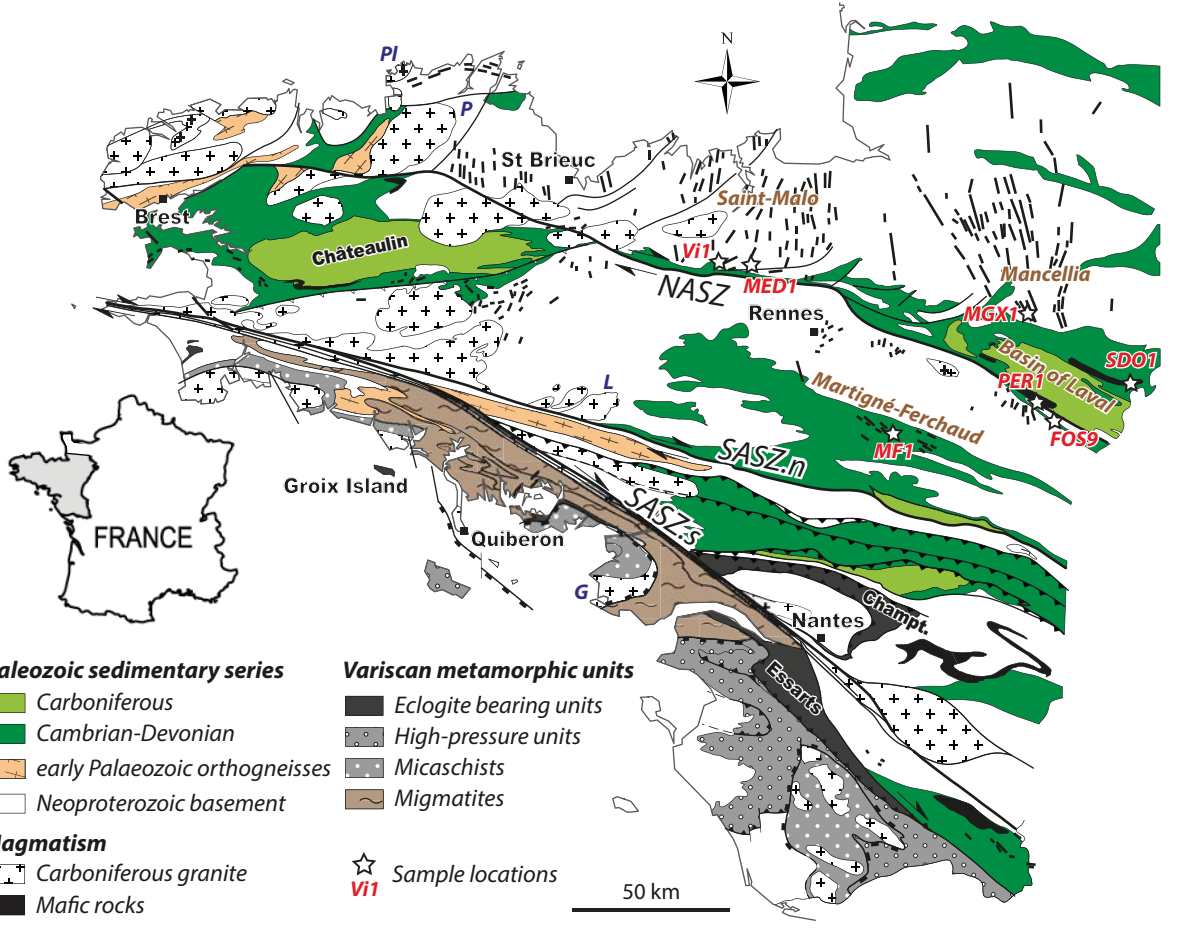

This is a preprint, the final version is subject to change, of the American Mineralogist (MSA)
Cite as Authors (Year) Title. American Mineralogist, in press.
(DOI will not work until issue is live.) DOI: http://dx.doi.org/10.2138/am-2016-5736

Figure 2

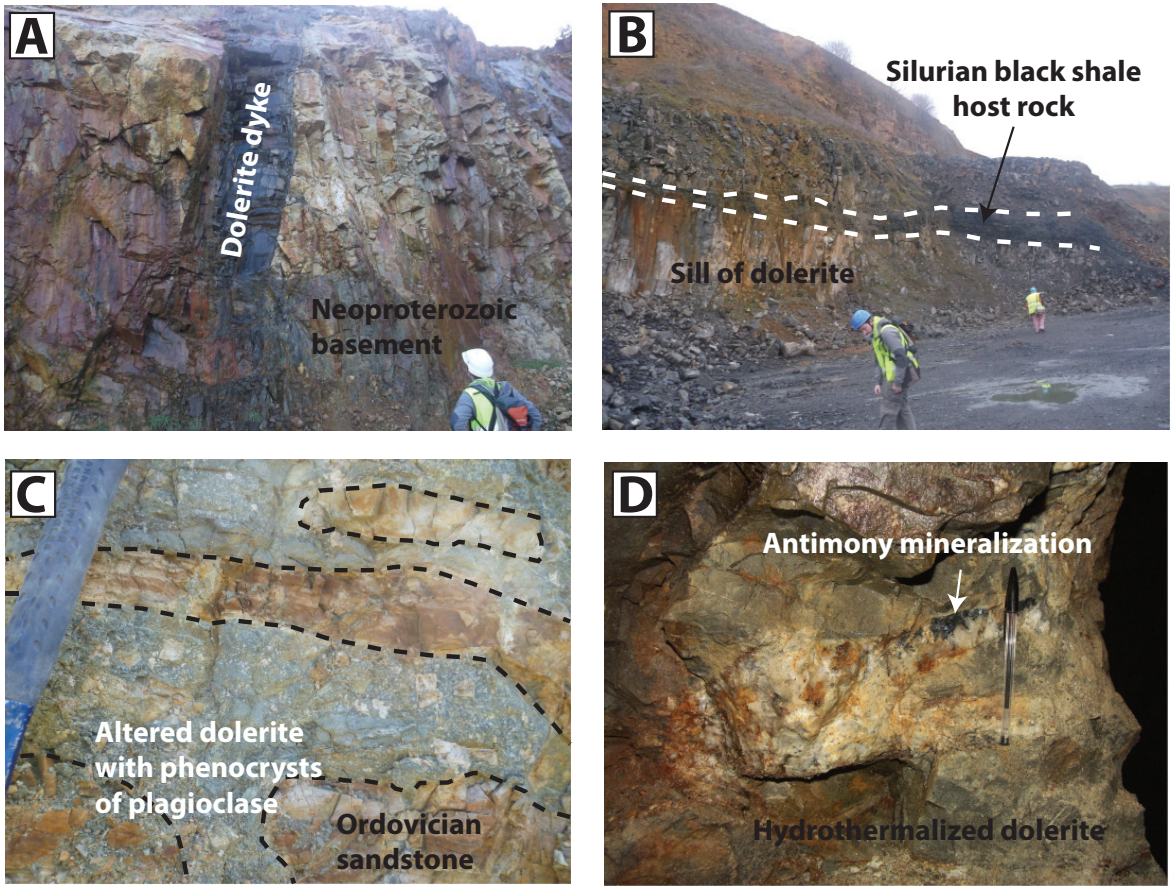

This is a preprint, the final version is subject to change, of the American Mineralogist (MSA)
Cite as Authors (Year) Title. American Mineralogist, in press.
(DOI will not work until issue is live.) DOI: http://dx.doi.org/10.2138/am-2016-5736

Figure 3

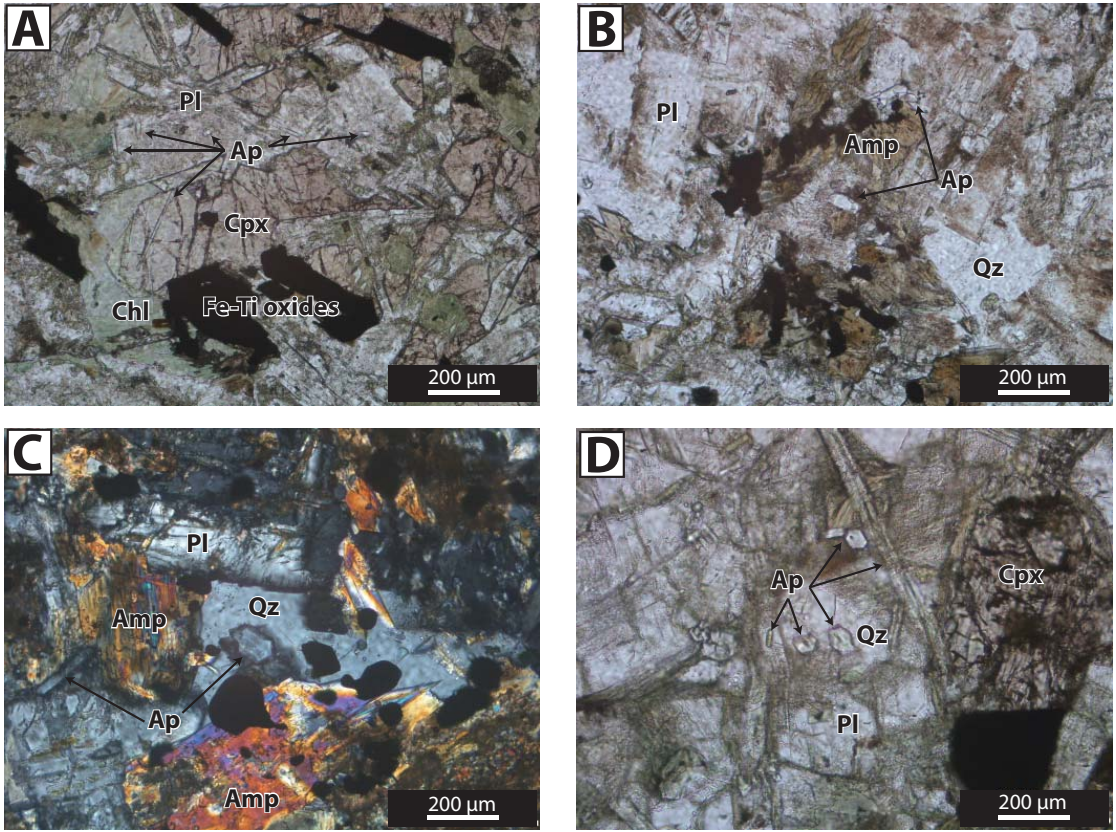

This is a preprint, the final version is subject to change, of the American Mineralogist (MSA)
Cite as Authors (Year) Title. American Mineralogist, in press.
(DOI will not work until issue is live.) DOI: http://dx.doi.org/10.2138/am-2016-5736

Figure 4

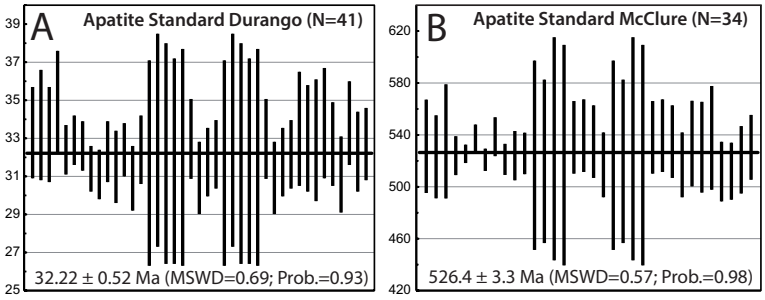

This is a preprint, the final version is subject to change, of the American Mineralogist (MSA)
Cite as Authors (Year) Title. American Mineralogist, in press.
(DOI will not work until issue is live.) DOI: http://dx.doi.org/10.2138/am-2016-5736

Figure 5

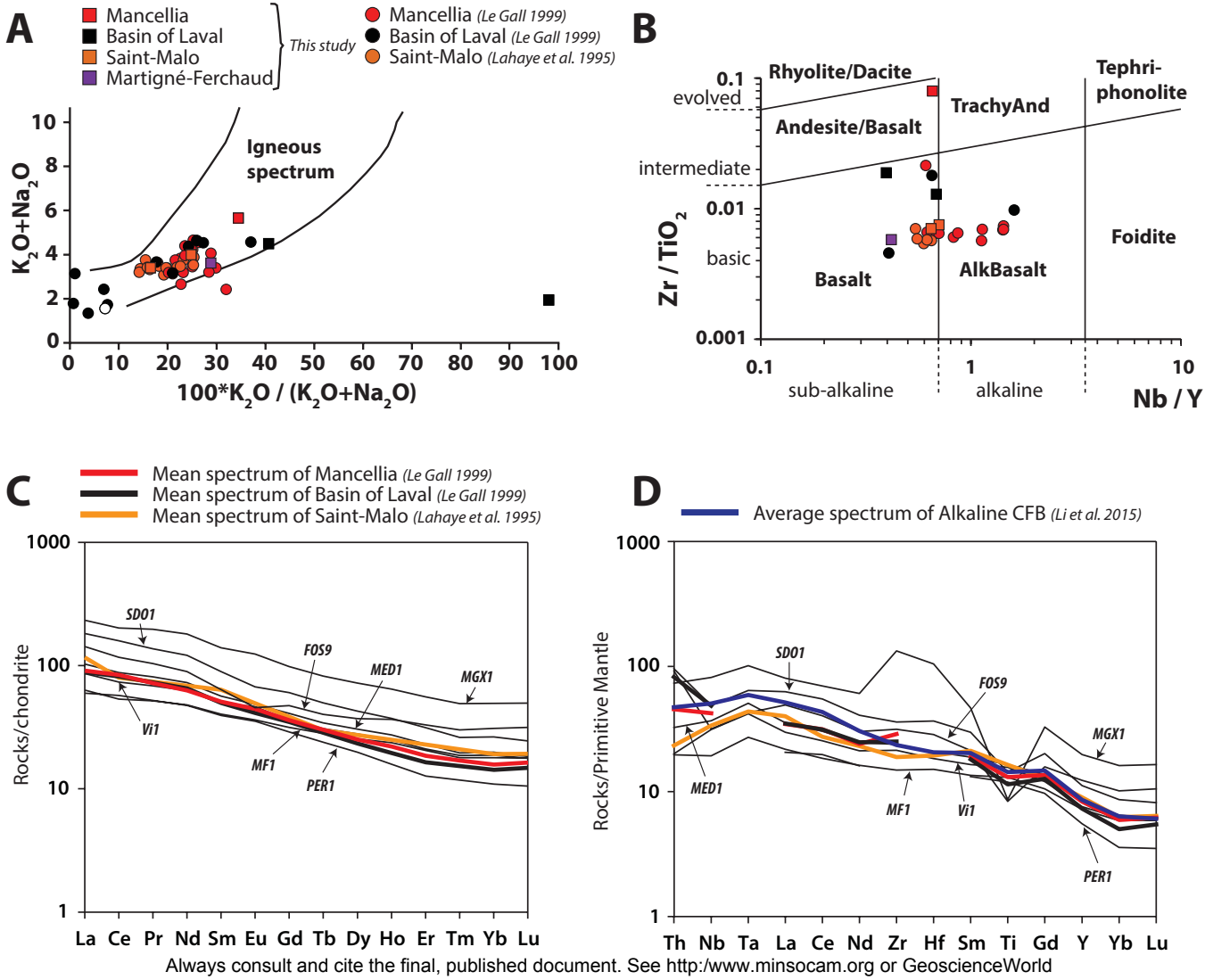

This is a preprint, the final version is subject to change, of the American Mineralogist (MSA)
Cite as Authors (Year) Title. American Mineralogist, in press.
(DOI will not work until issue is live.) DOI: http://dx.doi.org/10.2138/am-2016-5736

Figure 6

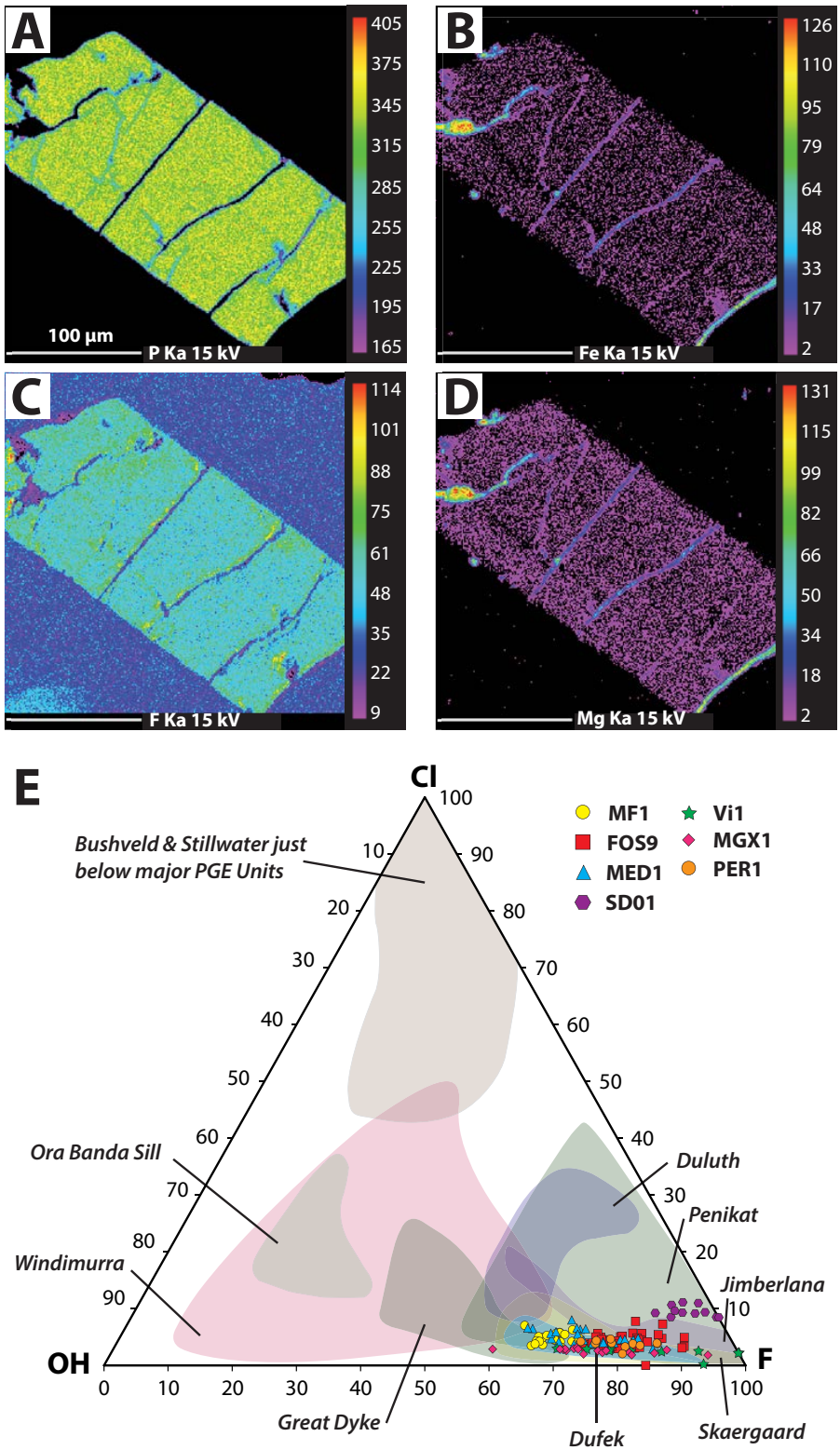

This is a preprint, the final version is subject to change, of the American Mineralogist (MSA)
Cite as Authors (Year) Title. American Mineralogist, in press.
(DOI will not work until issue is live.) DOI: http://dx.doi.org/10.2138/am-2016-5736

Figure 7

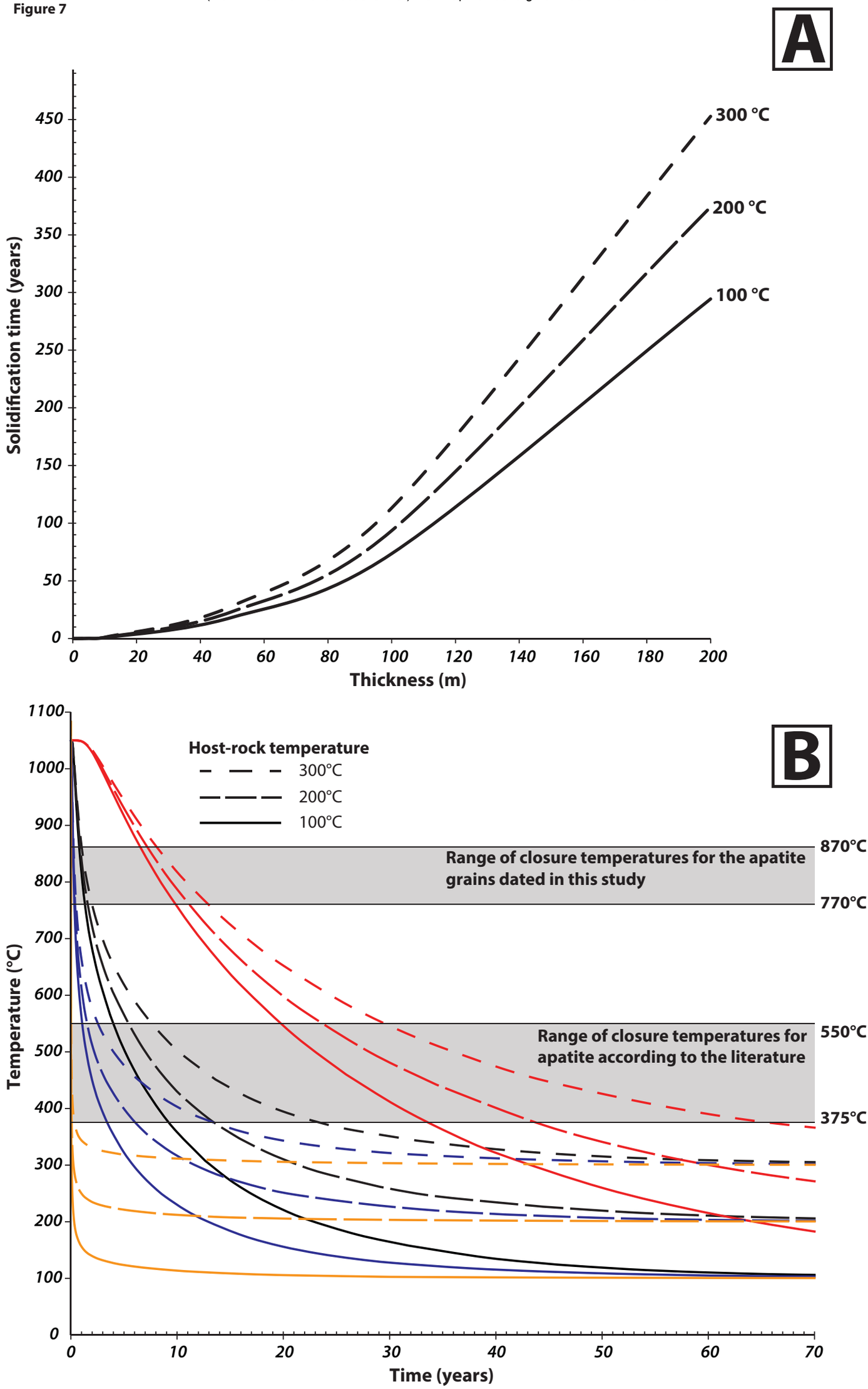

This is a preprint, the final version is subject to change, of the American Mineralogist (MSA)
Cite as Authors (Year) Title. American Mineralogist, in press.
(DOI will not work until issue is live.) DOI: http://dx.doi.org/10.2138/am-2016-5736

Figure 8

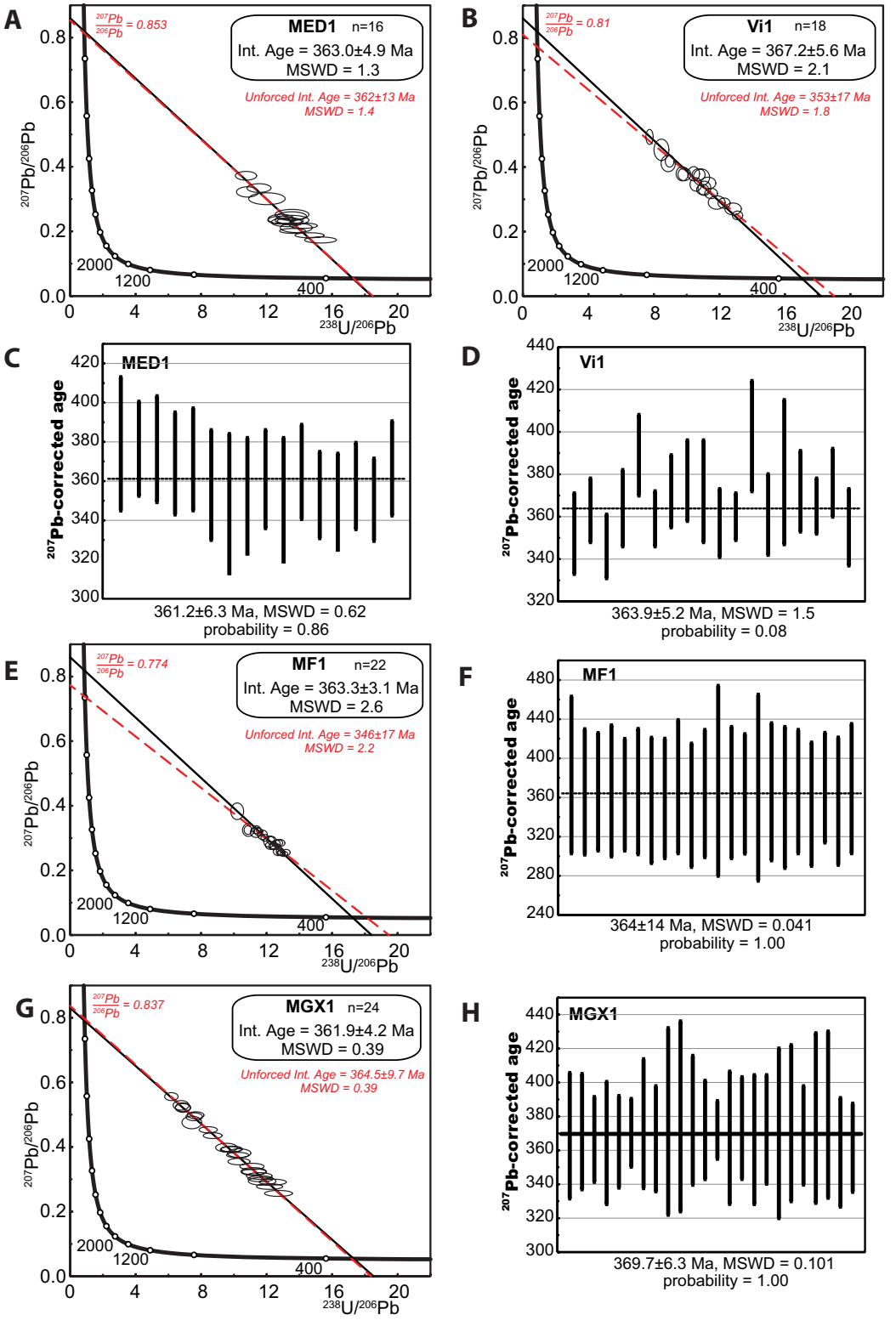

This is a preprint, the final version is subject to change, of the American Mineralogist (MSA)
Cite as Authors (Year) Title. American Mineralogist, in press.
(DOI will not work until issue is live.) DOI: http://dx.doi.org/10.2138/am-2016-5736

Figure 9